Physically-Based Modelling of co-seismic Landslide, Debris Flow and Flood Cascade

Bastian van den Bout[1], Chenxiao Tang[2], Cees van Westen[1], Victor Jetten[1]

[1]Faculty of Geo-Information Science and Earth Observation (ITC), University of Twente.

[2]Institute of Mountain Hazards and Environment, Chinese Academy of Sciences & Ministry of Water Conservancy.

Correspondence to: B. van den Bout (b.vandenbout@utwente.nl)

Abstract. The 2008 Wenchuan earthquake lead to various complex multi-hazard chains that included seismically-triggered landslide initiation, landslide run-out, river damming, dam breaching and flooding. The modelling of the interactions between such hazardous processes is challenging due to the complexity and uncertainty. Here we present an event-based physically-based model that is able to simulate multi-hazard land surface process chains within a single unified simulation. The final model is used to simulate a multi-hazard chain event in the Hongchun watershed, where co-seismic landslides led to a landslide dam and, two years later, a debris flow that breached the landslide dam. While most aspects of the multi-hazard chain are well predicted, the correct prediction of slope failures remains the biggest challenge. Although the results should be treated carefully, the development of such a model provides a significant progress in the applicability of multi-hazard chain simulations.

1 Introduction

Many of the damaging events that involve land surface processes are not caused by individual but multiple interacting hazardous processes. Such combinations can take place because the same triggering events (e.g. extreme rainfall) triggers various hazardous processes (e.g. flashfloods, landslides and debris flows) that interact and that may impact the same elements-at-risk. For multi-hazard assessment, the hazard intensities and impact can differ significantly when compared to the individual hazardous processes (Gill & Malamud, 2014; Van Westen and Greiving, 2017). Hazardous events may also occur in sequence as cascading or domino events whereby one hazardous process triggers another either directly or later in time. One particular

25 hazardous example of such cascading hazard events is the natural damming of rivers by landslides (Costa & Schuster, 1988; Walder & O'Conner, 1997). These landslide dams occur in mountainous landslide-prone areas around the world (Swanson et al., 1986; Chai et al., 2000; Dai et al. 2005; Korup, 2005; Harp and Crone, 2006; Nash et al., 2008; Liu et al., 2009; Fan et al., 2014). This sequence of hazardous events starts with a catastrophic slope failure, often caused by intense precipitation, a seismic trigger, or a combination of these. The released material moves downslope and can lose momentum through friction

30 or by entering a sharply incised channel or river. When the volume of the solid materials is large enough, or when the moved landslide body retains mostly its original strength characteristics, it will form a barrier for water flow which will accumulate to form a dammed lake. Depending on the strength of the materials composing the dam, the barrier may breach when the barrier lake level exceeds the height of the dam, either due to accelerated erosion, piping or barrier collapse (Ermini and Casagli, 2003). During the breach, extreme discharges and solid-laden floods with high velocity may devastate the downstream

35 areas (Schuster, 1993; Walder and O'Connor, 1997).

Natural dynamical systems such as the one described above can be complicated, containing many interactions and numerous fundamental processes related to hydrology and sediments (Walder & O'Conner, 1997). Slope failures, mass movement runout and flooding are influenced by catchment scale hydrology (van den Bout et al., 2018). Furthermore, inter-hazard interaction exist in many varieties, a review of which can be found in Kappes et al. (2012). In the case of landslide dam formation and

40 breaching, many interactions exist between processes that are typically approached individually in modelling. Landslide dam break floods have been analyzed using both empirical and physically-based models (Evans, 1986; Costa and Schuster, 1988; Peng and Zhang, 2012). Empirical models are simpler to apply but provide less comprehensive results than physically-based models. On the other hand, physically based models require detailed physical parameters as input, and can be computationally costly. Whereas the individual components of the hazard chain: landslide initiation, landslide run-out, dam breach and flooding,

45 have been modelled using physically-based models, the interactions between these processes are generally not simulated within a single model due to their high complexity.

The prediction of landslide volumes resulting from earthquakes is a complex problem, and requires specialized numerical models. Several physically-based simulation tools for slope failure volume modelling have been developd, such as CLARA (Hungr et al., 1989), TSLOPE3 (Pyke, 1991), 3D-SLOPE (Lam and Fredlund, 1993), 3-DSLOPEGIS (Xie et al., 2003),

2

50   r.slope.stability (Mergili et al., 2014), Scoops3D (Reid et al., 2015), EDDA (Chen & Zhang, 2015) and OpenLISEM (Van den Bout et al., 2018). CLARA, TSLOPE3, and 3D-SLOPE can only be applied on individual slopes, while r.slope.stability, Scoops3D, and OpenLISEM are spatially distributed models, which are based on Geographic Information Systems (GIS). These can be applied for landslide volume estimation over a large area up to several hundred km^2. Numerical modelling of mass movement run-out using 2-D approaches has been implemented in a variety of models (Malet et al., 2004; Rickenmann

55   et al., 2006; Van Asch et al., 2007; Hürlimann et al., 2007; Domenech et al., 2019). They need detailed information on initial volume, rheology, entrainment and an accurate and detailed digital elevation model (DEM) (Hürlimann et al 2007). Erosion, the water-driven uptake of sediment, and entrainment, the grain-driven uptake of sediment, have been used in understanding mass flow soil interactions. Erosion models, while traditionally focused on agricultural processes, come in great variety and provide insight into the flow-surface interactions. Examples are WEPP (Nearing et al., 1989), EUROSEM (Morgan et al.,

60   1998) and Delft3D Sediment (Roelvink and Banning, 1995).

In the case of multi-hazard chains including landslide dams, integrated simulations face several critical issues. When a mass movement enters a channel, with a certain water level, the landslide material mixes with the water in a dynamic manner, which is generally ignored in existing flow models such as Flo-2D (O'Brien et al., 1993). Similarly, the volumetric sediment content of water increases when a landslide dam is breached, and the material of the dam is entrained by the water flow. The

65   entrainment of bed material is simulated in a limited number of spatial two-dimensional mass movement models, but is rarely initiated from low-concentration water flow (Hungr et al., 2005). Several models have shown this functionality, but lack the capability of modelling breaching behavior, and ignore the resulting changes in the digital elevation model (Chen & Zhang, 2015; Hu et al.,2016; Baggio et al., 2021). Ignoring these changes makes the simulation of any breaching behavior impossible, since increasing outflow must be the result of the entrainment of a flow path on the landslide dam.

70   Simplified coupled model approaches have been tested using separate, and non-spatially distributed models for water flow and dam breaching. Empirical equations for dam-breach discharge have been developed and implemented by Singh & Snorasson (1984), Wang et al. (2008) and in the BREACH model (Fread, 1988). In these models, mathematical expressions for the dynamics of the outgoing discharge during a dam breach are derived from simplified landslide dam examples. Typically, a feedback loop between outflowing discharge and the amount of material entrained from the landslide dam determines the

75 dynamics of the hydrograph. While these provide a useful estimation of the relevant physical processes during a dam breach, only outgoing discharge is simulated and downstream processes are unknown. Moreover, the accuracy is generally low for more complicated cases (Zhu, 2006). The BREACH model simulates the increasing breach depth in a landslide dam using an iterative numerical solution. At the sides of the entrained channel, a limiting angle determines the additional collapse of material. Valiani et al. (2002) improved this by simulating dam breach discharge using a two-dimensional finite element
80 method.

Fan et al. (2014) provided an insightful step towards integrated modelling by linking an one-dimensional breach outflow model with a hydraulic 2D flood simulation. The outflow from the BREACH model determines the boundary condition for the flood model (Sobek). With this combined setup, it was possible to predict the dynamic dam breaching and the resulting large scale flood behavior, with significant accuracy. However, this integrated setup was still limited by the assumptions in the model.

85 The breach model is one-dimensional and uses a simplified shape for the estimation of breaching dynamics. The setup ignores catchment-scale hydrological processes that could influence the surface flow. Furthermore, breach outflow can typically contain large amounts of solid material, altering the dynamics of the mixture. Fan et al. (2014) implemented a flood model where flow is calculated using the Saint Venant equations for shallow flow, which ignores forces such as viscosity, and implements a fluid-based frictional model (Dhondia and Stelling, 2002). Li et al. (2011) provided a different approach to

90 integrated simulations of landslide dams by linking the BREACH model with both a regional rainfall-runoff model and the Flo-2D debris flow model for modelling the runout of the breach material. Despite their improved method, the landslide dam brech modelling depends on assumptions such as constant flow material properties, a limiting region for entrainment and landslide initiation coming from pre-defined boundary conditions. More recently, Mergili et al (2017) show the application of diluting mass flows to modelling Glacial Lake Outburst floods. They developed the r.avaflow model, based on two-phase

95 mixture equations by Pudasaini (2012) that allows for mixed flow of water and solids and implements a simplified entrainment process. However, this work does not take into account catchment-scale processes or actual landslide dam formation.

In this research, we aim to simulate a complex multi-hazard chain using a physically-based integrated model. We aim to present an updated version of the LISEM hazard model, and analyze the application of this model to complex co-seismic hazard chains. The model includes a complete spatial simulation of a landslide dam process chain, including initial slope failure, landslide

100   runout, deposition, lake formation, dam breaching and flooding. To test the behavior of the developed model, simulations and validation will be shown for a case study of a dam-break flood event in the Hongchun watershed, that occurred in 2010 near Yinxiu town, close to the epicenter of the 2008 Wenchuan earthquake, in Sichuan Province, China. Finally, we investigate the predictive capabilities of complex multi-hazard multi-stage simulation by analyzing the sensitivity of the model to changes in input parameters.

105   The investigation of the Hongchun watershed builds on previous works in literature. Tang et al. (2011; 2015) describe the co-seismic and post seismic landslide events between 2008 and 2011 in this area. Several other studies have simulated the event using a variety of modelling techniques. Ouyang et al. (2015) applied shallow flow depth-averaged debris flow equations in order to understand the event as a simplified runout process. Zhang et al., (2018) utilized a depth-averaged smooth particle hydrodynamics model to simulate both runout from landslides and the later debris flow. The authors show a novel application

110   of such methods to a multi-stage event, however, without an integration in catchment scale hydrology and a physical implementation of entrainment and breaching of the landslide dam. Domenech et al. (2019) used a multi-event debris flow model including entrainment to study the effect of material depletion on debris flow initiation in the Hongchun watershed. Using results of modelling studies, Chen et al. (2016) performed a cost-benefit analysis for the mitigation measures to protect the touristic town of Yinxiu, located directly opposite to the outlet of the Hongchun watershed on the other side of the Ming

115   River.

    In this research, there is a focus on the integrated nature of the developed multi-hazard model. Multi-hazard multi-stage behavior is simulated for a series of interacting earthquake, landslide, debris flow and flood processes in the Hongchun watershed. In order to simulate the behavior of this complex event, we develop an extended and improved version of OpenLISEM hazard. To analyze the uncertainties in modelling such process chains, we employ ensemble simulations and

120   analyze spatial hazard probabilities to estimate reliability. Finally, we discuss the benefits, downsides and potential application of modelling methods that involve integrated multi-hazard process chains.

2 Theoretical Model Background

This section presents the theoretical background and governing equations for the components of our multi-hazard model. One of the important cornerstones is the work by Pudasaini (2012) who developed a set of physically-based two-phase mass movement equations that can adapt the internal forces in the flow based on the local volumetric solid concentration. This allows to simulate the behavior of landslides, the flow of water and the interactions between mass movements and water flow (Mergili et al., 2018). Using these equations, van den Bout et al. (2018) developed an integrated model for slope hydrology, slope failure, mass movements and runout.

We have implemented a series of new processes within the physically-based OpenLISEM Hazard model. In this section, we describe relevant theory of existing functionality, as well as the addition of terrain-altering entrainment by mixture flows, and the simulation of co-seismic shallow landslides. An overview of the processes is provided in figure 1.
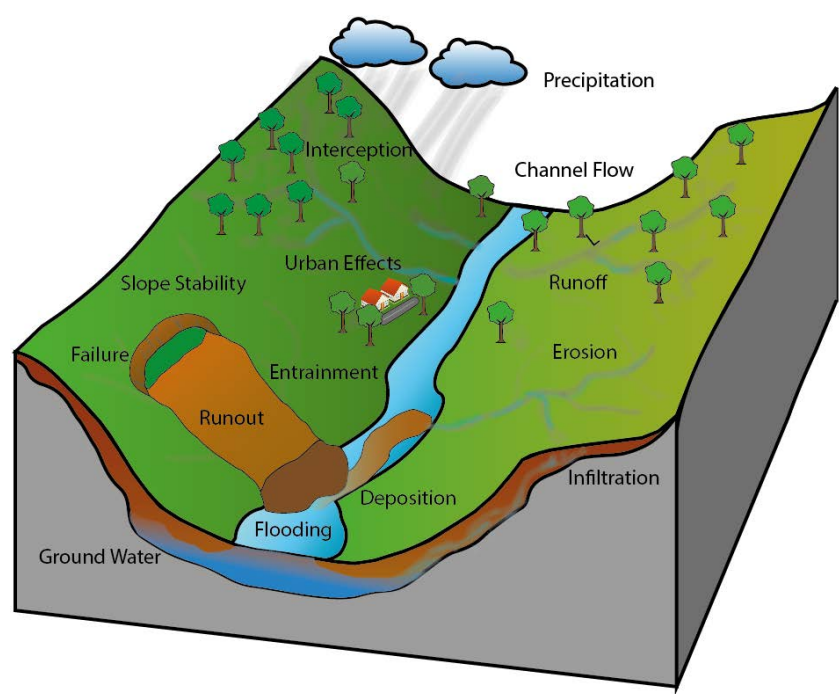

Figure 1 A schematic overview of processes, fluxes and storages within the OpenLISEM model.

1.1 Hydrology

6

The principle setup of the model starts with the surface aspects of the hydrological cycle. Spatially and temporally distributed rainfall forms the main input of water. We implement a set of equations for interception and micro-surface storage based on the original version of OpenLISEM (Jetten & de Roo, 2004; Baartmans et al., 2013). The Green & Ampt infiltration model is

140 implemented, which assumes a wetting front moving down into the soil due to infiltrating rainfall (Green & Ampt, 1911). The resulting potential infiltration is subtracted from the available surface water (Equation 1).

1
$$f_{pot} = -K_s \left(\psi \frac{\theta_s - \theta_i}{F} + 1 \right)$$

Where f_{pot} is the potential infiltration rate $(m\ s^{-1})$, F is the cumulative infiltrated water (m), θ_s is the porosity $(m^3\ m^{-3})$, θ_i is the initial soil moisture content $(m^3\ m^{-3})$, ψ is the matric pressure at the wetting front $(h = \psi + Z)$

145 (m) and K_s is the saturated conductivity $(m\ s^{-1})$.

A separate modelling component is used to simulate several months of groundwater dynamics and generate the initial ground water conditions for the OpenLISEM Hazard simulation, which silumates the effects of a single rainstorm. Groundwater flow is estimated using a depth-averaged Darcy equation (Equation 2), as is common in regional hydrological models (Van Beek, 2002).

150 2
$$V_d = K_s * \frac{dh}{dx}$$

Where h is the hydraulic head (m) and V_d is the darcy flow velocity $(m\ s^{-1})$

1.2 Slope Stability and Failure

Hydrology influences slope stability and can eventually lead to failure. Slope failure is based on the Iterative Failure Method (Bout et al., 2018). This technique reverses the Factor of Safety (equation 3) to solve for the remaining depth of material at

155 which the local situation becomes stable. The locally altered terrain then results in changed forces in the surrounding cells. Through iteration, the method keeps removing material until no unstable cell is left and the minimum required material for a stable terrain has been removed. We added the seismic forcing in the Factor of Safety calculation following Morgenstern & Sangrey (1978).

3
$$FOS = \frac{c' + (((\gamma - m\gamma_w)h_s + m\gamma_w z)cos(\beta)^2 - h_s\gamma\alpha sin(\beta)\cos(\beta)\ )\ tan(\phi)}{((\gamma - m\gamma_w)h_s)sin(\beta)\cos(\beta) + h_s\gamma\alpha cos(\beta)^2}$$

160 Where FOS is the Factor of Safety (-), β is the slope of the soil section (-), c' is the apparent cohesion of the soil (kPa), α is the peak horizontal earthquake acceleration $(m\ s^{-2})$, ϕ is the internal friction angle of the soil (-), γ is the density of the slope material $(kg\ m^{-3})$, γ_w is the density of water $(kg\ m^{-3})$, m is the fraction of the soil depth that is saturated from the basal boundary (-) and h_s is the depth of the failure plane (m).

165 The apparent cohesion consists of additional root cohesion and a matric suction term. The acceleration is assumed to be, as in the most critical situation, the estimated peak horizontal ground acceleration. To account for sub-surface force propagation, we include an iterative force solution. This is an extension of similar approaches in Zhou & Cheng (2013) and Zhou et al., (2014). In the proposed implementation, forces are iteratively solved throughout the entire terrain description (Figure 2).
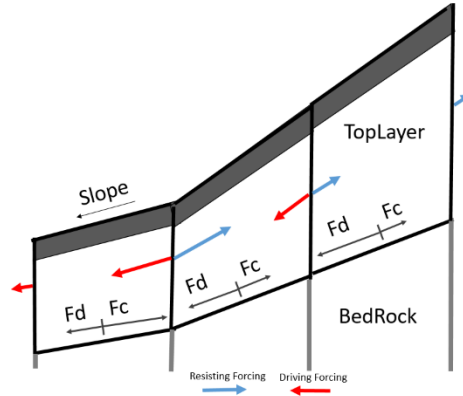

170

Figure 2 Sub-surface force distribution is solved through iteratively finding a steady state (Fd = driving force, Fc = resisting force)

In the three-dimensional case, where the x-and y- components of the seismic forcing and slope steepness influence the propagation, this can be expressed as equation 4.

175

4
$$\nabla \overrightarrow{F_{up}} + \left(\vec{C} - \vec{D}\right) * \left(\vec{S} \cdot \overrightarrow{F_{lat}}\right) = 0$$

With C the force capacity (numerator of equation 3), D the force demand (denominator of equation 3), $\vec{S}$ is the normalized slope vector (-) and $\overrightarrow{F_{lat}}$ is the vector of laterally acting forces ($kg\ m\ s^{-2}$).

180   We assume that excess force is transferred downslope, but the fractured top material is unable to transfer force resistance upslope.

We assume in the set-up of the model that a failure plane can develop in the soil materials at any depth. Equation 3 can be inverted to find the value of h, for which the safety factor is one. To solve this equation for h, we first express the slope based on the local elevation differences and create a shortened equation for the factor of safety (equation 5 and 6).

185

5
$$\beta = atan\left(\frac{\max\ (z_{x-1}-z_x, z_x-z_{x+1})}{dx}\right)$$

6
$$FOS = 1 = \frac{C_1 + C_2 \cdot \cos\left(atan\left(\frac{z-z_0}{dx}\right)\right)^2 \cdot \tan(\phi)}{C_3 \cdot \sin\left(atan\left(\frac{z-z_0}{dx}\right)\right) \cdot \cos\left(atan\left(\frac{z-z_0}{dx}\right)\right)}$$

Where the simplified constants are given by equations $C_1 = c$, $C_2 = (((\gamma - m\gamma_w)h_s + m\gamma_w h_s)$, $C_3 = ((\gamma - m\gamma_w)h_s)$, β is the slope angle (-), z is the elevation above the failuresurface (m) and z_0 is the lowest neighboring elevation (m).

190   Solving this equation can be done using the trigonometric identities (Equation 7 and 8).

7
$$\cos(atan(x)) = \frac{1}{\sqrt{1+x^2}}$$

8
$$\sin(atan(x)) = \frac{x}{\sqrt{1+x^2}}$$

Finally, we find the lowest real root to the second-order polynomial equation of the form

9
$$h_s = a + (b)\ x + (c)x^2$$

195   Where

10
$$a = C_1\ h_0^2 - C_1\ dx^2$$

11
$$b = 2\ C_1 h0 - C_3\ h_0\ FOS - C_3 h_0 FOS\ dx\ C_2 dx^2$$

12
$$c = C_1 - C_3\ FOS\ dx$$

Using equation 9 the critical depth can be found, where the material on the slope is in equilibrium. By multiplying the area of

200   a pixel with the slope material height above this critical depth, a failure volume can be calculated. This volume consists of

solids and water, depending on the soil saturation level, and is then added to the flow equations that simulate Mohr-Coulomb mixture flow.

1.3 Flow Dynamics

Once a volume of flowing material is introduced (either through hydrology or slope failure), its movement must be described. The dynamics of mass and momentum are calculated using a discretization of the continuity equation for mass and momentum of both solids and fluids (Equation 13, 14 and 15). Equation 13 described the conservation of mass, and equation 14 describes conservation of momentum. On the left hand side the storage term and advective terms are found. External forces and mass sources are added on the right hand side.

13
$$\frac{\partial h}{\partial t} + \frac{\partial (hu_x)}{\partial x} + \frac{\partial (hu_y)}{\partial y} = R - I$$

14
$$\frac{\partial hu_x}{\partial t} + \frac{\partial (hu_x^2)}{\partial x} + \frac{\partial (hu_x u_y)}{\partial y} = \boldsymbol{gh(S_x - S_{f,x})}$$

15
$$\frac{\partial hu_y}{\partial t} + \frac{\partial (hu_y^2)}{\partial y} + \frac{\partial (hu_x u_y)}{\partial x} = \boldsymbol{gh(S_y - S_{f,y})}$$

With h being the flow height (m), u the flow velocity $(m\ s^{-1})$, R the rainfall (m), I the infiltration (m), g the gravitational acceleration $(m\ s^{-2})$, S the friction term $(m\ s^{-2})$ and S_f the momentum source term $(m\ s^{-2})$.

The momentum source terms predominantly determine the behavior of the flow. Here we implement pressure and friction forces for fluids as is typical for shallow water assumptions (O'Brien et al., 1993).

16
$$S_x = -\frac{d\left(\frac{gh^2}{2}\right)}{dx} - ghS_{f_x}$$

17
$$S_y = -\frac{d\left(\frac{gh^2}{2}\right)}{dy} - ghS_{f_y}$$

The friction slope terms, which are the friction forces divided by the water height and the gravitational acceleration, can be calculated using the Darcy-Weisbach friction law (Chow, 1959) (Equation 16).

18
$$S_f = \frac{g}{n^2} \frac{\bar{u}|\bar{u}|}{h^{\frac{4}{3}}}$$

With n the Manning's n friction coefficient $(s\ m^{-\frac{1}{3}})$.

The momentum source terms within OpenLISEM Hazard are based on the work by Pudasaini (2012). This set of equations contains a physically-based two-phase momentum balance. Besides pressure and gravitational forces, it includes viscous forces, non-Newtonian viscosity, two-phase drag and a Mohr-Coulomb type friction force for the solid phase (Equations 19, 20, 21, 22). Based on the current and local state of flow, forces change in magnitude. This approach allows for a smooth transition between non viscous flow, hyper concentrated streamflow, debris flows or landslide runout by automatically scaling and solving the interactions between solids and fluids.

19
$$S_{x,s} = \alpha_s \left(g\left(\frac{\partial b}{\partial x}\right) - \frac{u_s}{|\vec{u}_s|}\tan(\partial P_{b_s}) - \varepsilon P_{b_s}\left(\frac{\partial b}{\partial x}\right) \right) - \varepsilon \alpha_s \gamma P_{b_f}\left(\frac{\partial h}{\partial x} + \frac{\partial b}{\partial x}\right) + C_{DG}(u_f - u_s)|\vec{u}_f - \vec{u}_s|^{j-1}$$

20
$$S_{y,s} = \alpha_s \left(g\left(\frac{\partial b}{\partial y}\right) - \frac{v_s}{|\vec{u}_s|}\tan(\partial P_{b_s}) - \varepsilon P_{b_s}\left(\frac{\partial b}{\partial y}\right) \right) - \varepsilon \alpha_s \gamma P_{b_f}\left(\frac{\partial h}{\partial y} + \frac{\partial b}{\partial y}\right) + C_{DG}(v_f - v_s)|\vec{u}_f - \vec{u}_s|^{j-1}$$

21
$$S_{x,f} = \alpha_f \left\{ g\left(\frac{\partial b}{\partial x}\right) - \varepsilon \left[\frac{1}{h}\frac{\partial}{\partial x}\left(\frac{h^2}{2}P_{b_f}\right) + P_{b_f}\frac{\partial b}{\partial x} - \frac{1}{\alpha_f N_R}\left(2\frac{\partial^2 u_f}{\partial x^2} + \frac{\partial^2 v_f}{\partial y \partial x} + \frac{\partial^2 u_f}{\partial y^2} - \frac{\chi u_f}{\varepsilon^2 h^2}\right) + \frac{1}{\alpha_f N_R}\left(2\frac{\partial}{\partial x}\left(\frac{\partial \alpha_s}{\partial x}(u_f - u_s)\right) + \right. \right. \right.$$

$$\left. \left. \left. \frac{\partial}{\partial y}\left(\frac{\partial \alpha_s}{\partial x}(v_f - v_s) + \frac{\partial \alpha_s}{\partial y}(u_f - u_s)\right)\right) - \frac{\xi \alpha_s(v_f - v_s)}{\varepsilon^2 \alpha_f N_{R_A} h^2} \right] \right\} - \frac{1}{\gamma}C_{DG}(u_f - u_s)|\vec{u}_f - \vec{u}_s|^{j-1}$$

22
$$S_{y,f} = \alpha_f \left\{ g\left(\frac{\partial b}{\partial y}\right) - \varepsilon \left[\frac{1}{h}\frac{\partial}{\partial y}\left(\frac{h^2}{2}P_{b_f}\right) + P_{b_f}\frac{\partial b}{\partial y} - \frac{1}{\alpha_f N_R}\left(2\frac{\partial^2 v_f}{\partial y^2} + \frac{\partial^2 u_f}{\partial y \partial x} + \frac{\partial^2 v_f}{\partial y^2} - \frac{\chi v_f}{\varepsilon^2 h^2}\right) + \frac{1}{\alpha_f N_R}\left(2\frac{\partial}{\partial y}\left(\frac{\partial \alpha_s}{\partial y}(v_f - v_s)\right) + \right. \right. \right.$$

$$\left. \left. \left. \frac{\partial}{\partial y}\left(\frac{\partial \alpha_s}{\partial y}(u_f - u_s) + \frac{\partial \alpha_s}{\partial x}(v_f - v_s)\right)\right) - \frac{\xi \alpha_s(u_f - u_s)}{\varepsilon^2 \alpha_f N_{R_A} h^2} \right] \right\} - \frac{1}{\gamma}C_{DG}(u_f - u_s)|\vec{u}_f - \vec{u}_s|^{j-1}$$

With S_s is the momentum source term for solids ($m\ s^{-2}$) S_f is the momentum source term for fluids ($m\ s^{-2}$), α_s and α_f the volume fraction for solid and fluid phases (-), P_b the pressure at the base surface ($Kg\ m^{-1}s^{-2}$),b the basal surface of the flow (m), N_R the Reynolds number (-), N_{R_A} the quasi-Reynolds number (-), C_{DG} the drag coefficient (-), ρ_f is the density of the fluid ($kg\ m^{-3}$), ρ_s is the density of the solids ($kg\ m^{-3}$), γ the density ratio between the fluid and solid phase(-), χ the vertical shearing of fluid velocity ($m\ s^{-1}$), ε the aspect ratio of the model (-), ξ the vertical distribution of α_s (m^{-1}).

11

Our model follows the equations by Pudasaini (2012) for the definitions of the regular and interface Reynolds number, which represents the ratio between inertial and viscous forces within the fluid (Equation 23 and 24).

245   23
$$N_R = \frac{\sqrt{gLH}\rho_f}{\alpha_f \eta}$$

24
$$N_{R_A} = \frac{\sqrt{gLH}\rho_f}{A\eta}$$

Where L is the length scale of the flow (m), H is the height of the flow (m), η is the viscosity ($kg\ s^{-1}\ m^{-1}$) and A is the mobility of the interface, scaling parameter for non-Newtonian viscous-fluid stresses ($\approx 1 - \alpha_s$) (-).

250   To apply these two-phase equations successfully in a catchment-based model, we replace the frictional force for the water phase with the Darcy-Wiesbach equation for water flow friction. To complete the set of equations that govern debris flow-dynamics, several flow properties were estimated based on the volumetric sediment content. Viscosity is based on an empirical relation by O'Brien and Julien (1985) (Equation 25).

25
$$\eta = \alpha e^{\beta \alpha_s}$$

255   Where α_s is the volumetric solid content of the flow (-), α is the first viscosity parameter (-) and β the second viscosity parameter (-).

The drag coefficient is based on the relation provided by Pudasaini (2012) (Equation 26, 27, 28 and 29).

26
$$C_{DG} = \frac{\alpha_f \alpha_s \left(1 - \frac{\rho_f}{\rho_s}\right)}{\varepsilon U_T (PF(Re) + (1-P)G(Re))}$$

27
$$Re = \frac{\rho_f d U_T}{\eta_f}$$

260   28
$$F = \frac{\rho_f}{180\ \rho_s} \left(\frac{\alpha_f}{\alpha_s}\right)^3 Re$$

29
$$G = \alpha_f^{M(Re)-1}$$

12

Where F and G are the scalar functions describing the flow velocity of solids and fluids respectively (-), Re is the particle Reynolds number (-),d is the median grain diameter (-), U_T the settling velocity ($m\,s^{-1}$) and M is an empirical parameter depending on the Reynolds number (≈ 0.2) (-).

265 Finally, the settling velocity of small (d < 100 μm) grains is estimated by Stokes equations for a homogeneous sphere in water (Stokes, 1850). For larger grains (> 1mm),the equation by Zanke (1977) is used (Equation 30).

$$30 \qquad U_T = 10\,\frac{\frac{\eta}{\rho_f}^2}{d}\left(\sqrt{1+\frac{0.01\left(\frac{(\rho_s-\rho_f)}{\rho_f}gd^3\right)}{\frac{\eta}{\rho_f}}}-1\right)$$

In which U_T is the settling (or terminal) velocity of a solid grain ($m\,s^{-1}$), η is the dynamic viscosity of the fluid (), ρ_f is the density of the fluid ($kg\,m^{-3}$), ρ_s is the density of the solids ($kg\,m^{-3}$), d is the grain diameter (m)

270

1.4 Deposition and Dam-Formation

Flows such as the ones described by the equations presented above have complex interactions with the basal surface. In particular, material in the flow can be deposited, or material from the terrain can be entrained. Deposition occurs when the flow velocities of a solid-fluid mixture have sufficiently low velocities and drag forces are insignificant compared to shear

275 resistance. Then, water and solids are subtracted from flow volumes to form a saturated deposits layer. Further deposition occurs as an active process, during flow, based on the deposition equations of Takahashi (1992). These equations use local stability analysis and the ratio between the flow velocity and the critical velocity to estimate deposition of solids (Equation 31, 32, 33 and 34). Using these generalized deposition equations, a variety of more specific deposition-based processes can be potentially simulated. For example, deposition of landslide material in a river would equate to landslide dam formation in

280 rivers.

$$31 \qquad D = \left(1-\frac{|\vec{u}|}{p|\vec{u}|_{cr}}\right)\frac{\alpha_{eq}-\alpha}{\alpha^b}V$$

$$32 \qquad |\vec{u}|_{cr} = \frac{\frac{2}{5d_{50}}\sqrt{\frac{gsin(\theta_c)\rho}{0.02\rho_s}}1}{\left(\frac{\alpha^b}{\alpha}\right)^{-\frac{1}{3}}-1}h^{1.5}$$

13

33
$$\tan(\theta_c) = \frac{\alpha(\rho_s - \rho_w)\tan(\phi^b)}{\alpha(\rho_s - \rho_w) + \rho_w}$$

34
$$\alpha_{eq} = \frac{\rho_w \tan(\theta)}{(\rho_s - \rho_w)(\tan(\phi^b) - \tan(\theta))}$$

Where D is the deposition rate $(m\ s^{-1})$, $|\vec{u}|_{cr}$ is the critical velocity for deposition $(m\ s^{-1})$, p is the calibration factor for the critical velocity for deposition (-), α_{eq} is the equilibrium volumetric solid concentration (-), α^b is the volumetric solid concentration of the bed material (-), and d_{50} is the median grain size (m).

1.5 Entrainment Equations

In order to estimate entrainment, we implement the equations by Takahashi et al. (1992) in a similar manner as was done in the Edda model (Chen and Zhang, 2015). The expressions for the entrainment rate are provided by equation 35, 36 and 37.

35
$$E = K(\tau - \tau_c)$$

36
$$\tau = \rho g h S_f$$

37
$$\tau_c = c^b + (1 - C_s)\alpha(\rho_s - \rho_w)gh\ cos(\theta)^2 \tan(\phi^b)$$

Where E Is the rate of change of the basal topography (erosion rate) (ms^{-1}); τ is the shear stress (Pa), τ_c is the critical shear stress (Pa), S_f is the surface friction term (-), τ_y is the yield stress (Pa), K is the resistance parameter for laminar flow (-), n_{td} is the turbulent dispersive coefficient $(m^{\frac{1}{2}}s^{-1})$, c^b is the cohesion of the bed material (Pa) and C_s is the coefficient of suspension (-).

The surface shear term is calculated from the momentum conservation equation as the sum of all surface frictional terms. We adapt the expressions to conform to the momentum jump boundary condition, as provided by Iverson and Ouyang (2015) (Equation 38).

38
$$\frac{dz}{dt} = E = \frac{\tau - \tau_c}{\rho_{eff} u_b}$$

Where ρ_{eff} is the total effective density of the flow $(kg\ m^3)$, u_b is the basal velocity $(m\ s^{-1})$.

Iverson and Ouyang indicate that the equations by Takahashi et al. (1992) do not include a distinction between basal and mean velocities and do not conserve momentum. The basal velocity differs from the mean velocity of the flow according to a vertical velocity profile. Our model description does not include an estimate of the basal flow velocity. Therefore, we use the

entrainment coefficient as a scaling device to convert from the mean velocity to a basal velocity ($u_b \approx K \bar{u}$), with $\bar{u}$ the depth-averaged velocity of the flow. This approach was similarly taken by Pudasaini and Fischer (2016). Therefore,

$$39 \qquad \frac{dz}{dt} = E \approx \frac{\tau - \tau_c}{\rho_{eff} K \bar{u}}$$

Furthermore, we ignore vertical velocities in the model setup, a both common and necessary assumption that has given good
310   results in other models (Iverson and Ouyang, 2015). Finally, we alter the mass and momentum source terms to include the produced mass and momentum from entrainment and thereby hold to conservation of these quantities. We introduce into the flow, based on the entrainment rates, a new mixture of solids and fluids. The momentum of the flowing material is additionally increased by adding the momentum of the entrained mass, which gains a velocity equal to the estimated basal velocity. Lateral entrainment includes collapse due to slope failure which is included by solving for stable depth. This is automatically solved
315   by the iterative failure method as described previously. Slope failure is based on a local safety factor estimation which is inverted as is done for slope stability.

1.6 Flowchart and numerical implementation

A flowchart of the full model is given in figure 3. Hydrology forms the basis of the simulated cycle. From this, other sediment and solids-related processes are linked. At each timestep, properties of the flow are determined based on the actual water and
320   solid content. Furthermore, solid properties such as density, friction angle and size are advected with the solids. The flowcharts indicates the data required for each step of the simulation. This highlights the downside of integrated modelling approaches, the increase in required input data.
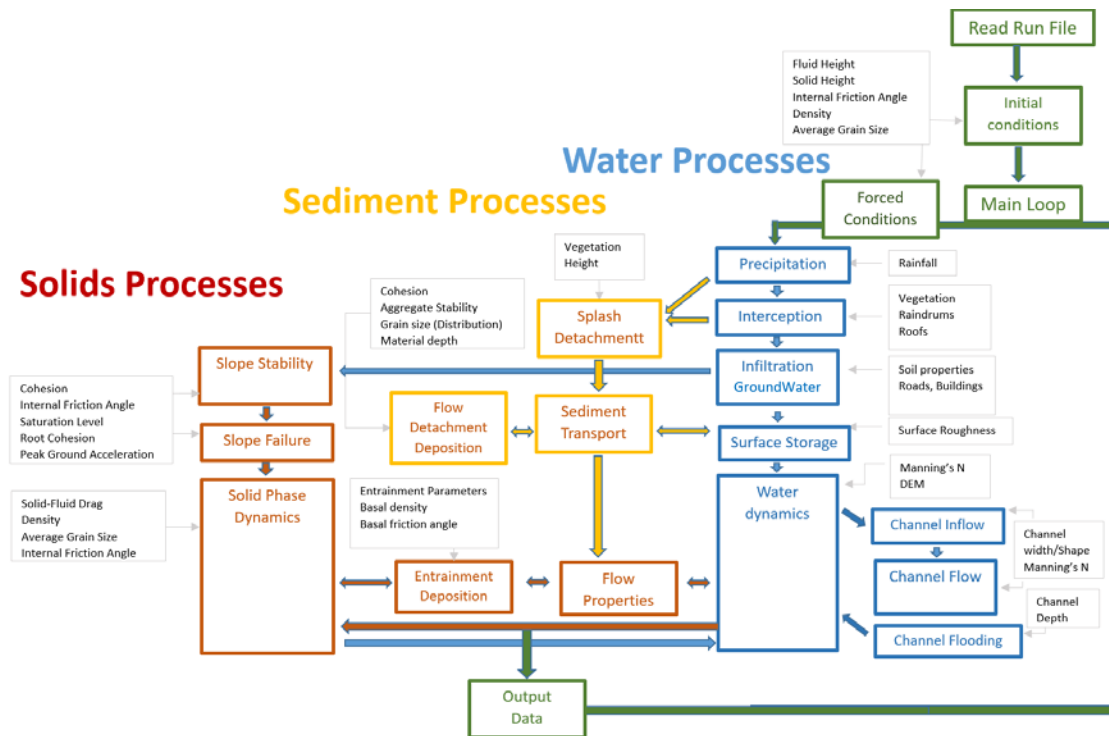
15

Figure 3 A schematic overview of the OpenLISEM Hazard model, including the link with the most relevant input data.

325 Similar catchment-integrated simulations that include hydrology, entrainment and debris flow initiation have been used

successfully by the EDDA model (Chen & Zhang, 2015), Hu et al. (2016) and by the STREP TRAMM model (Lehmann and

von Rütte, 2017). These models predict entrainment of slope material or landslide deposits, but do not alter the elevation

model. By using recent developments in numerical schemes, elevation model changes can be simulated without erroneous

feedbacks between terrain and flow. The numerical scheme within the model is based on the monotonic upstream cell-centered

330 scheme (MUSCL) (Van Leer, 1979). This scheme uses piecewise linear reconstructions of both the terrain surface and the

flow properties. This terrain reconstruction estimates local slope, and in rough terrain, also includes cell boundary elevation

differences. Besides shear stress from the bottom surface in a cell, cell boundary barriers can also provide shear resistance to

the flow. Our implementation of entrainment therefore takes into account direct and lateral entrainment.

3 Study Case

335   The integrated OpenLISEM multi-hazard model was applied in the Hongchun watershed, located near Yingxiu town in the
       epicentral area of the 2008 Wenchuan earthquake, in Sichuan province, China. This watershed experienced numerous co-
       seismic landslides and a catastrophic debris flow event in 2010. The debris flow deposits from this watershed dammed the
       main Min River and flooded Yinxiu town (Figure 4).

       This watershed has an area of 5.3 km^2, and elevation ranges between 900 and 1700 meters. The very steep slopes of this
340   watershed (>30 degrees slope for more than 86 percent of the catchment) were covered by dense forests before the earthquake
       in 2008. The steep terrain and sharply incised channels provide few locations for human settlements. The touristic town of
       Yinxiu is located adjacent to the Min river, and opposite of the outlet of Hongchun watershed. The lithology of the area
       consists mainly of highly fractured granitic rocks, with some pyroclastic rocks, limestones and sandstones (Tang et al., 2011).
       The texture of the weathered material is predominantly clay-loam with large amounts of gravel. The Beichuan thrust fault runs
345   straight through the watershed (Figure 4; Mahodja et al., 2016). In 2008, the fault was ruptured in the Wenchuan earthquake
       (M_w 7.9). After the earthquake, numerous landslides occurred in the area, leaving large volumes of deposits in the streams and
       channels, and removing the vegetation in 50% of the area. A detailed co-seismic landslide inventory from Tang et al. (2016)
       is shown in figure 4. The northern part of the catchment, which is part of the hanging wall, was more impacted than the southern
       part. One of the largest landslides in the watershed blocked the main channel of the Hongchun catchment (Figure 4), with the
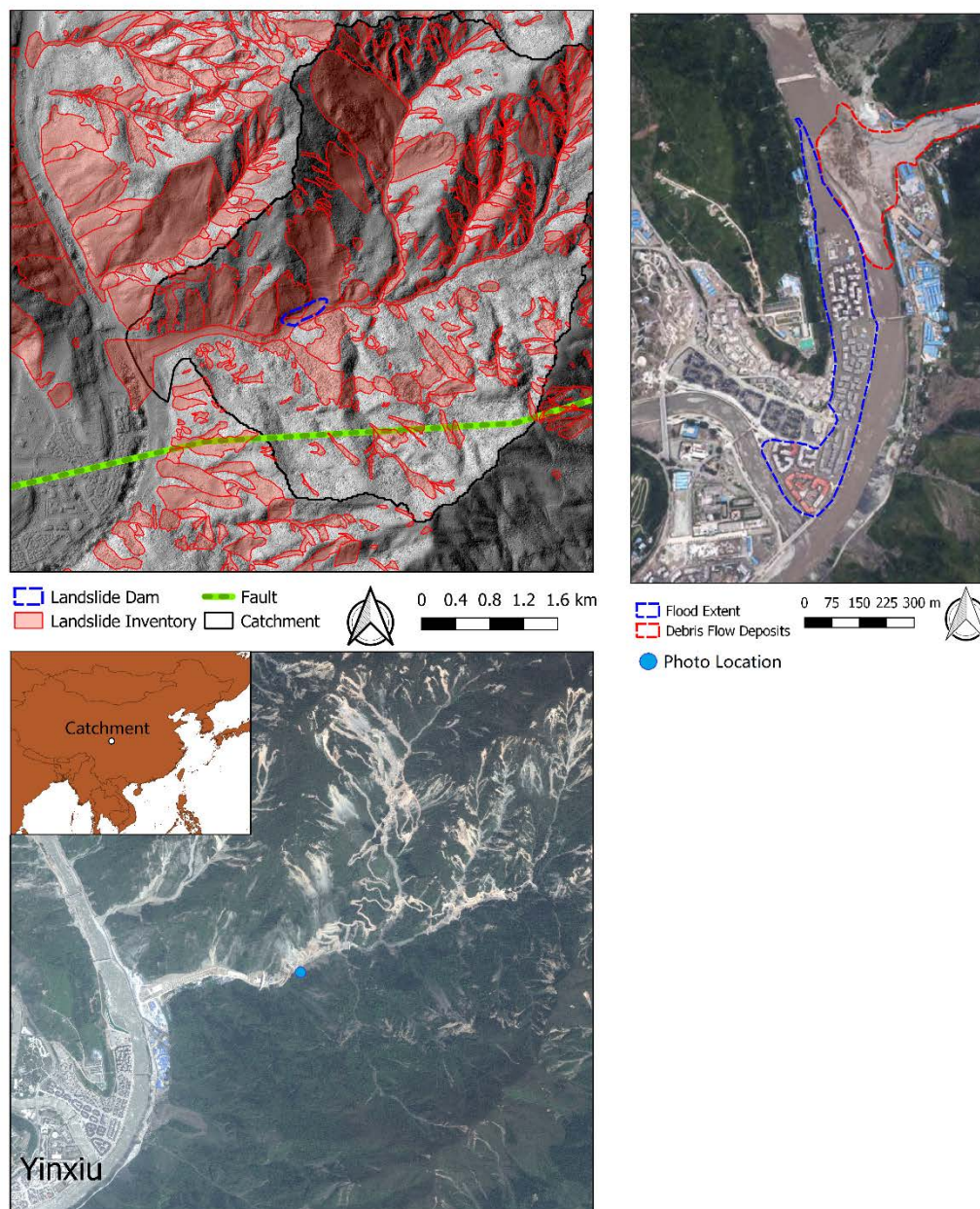350   deposits exceeding 8 meters in depth, and 70 meters in width.

Figure 4 An overview of the Hongshun Watershed: (Top) Hillshade Image with co-seismic landslide map from Tang et al. (2016) (bottom) Post-Event natural colour composite from Pléiades satellite, showing the situation in 2017. The construction of massive debris flow mitigation works in the outlet of the watershed are clearly visible, as is the continued mass movement activity, 9 years after the earthquake. (right) Aerial image of the 2010 debris flow blocking the Min river and causing flooding in Yinxiu town.

3.1 The Multi-Hazard Event of 2010

In 2010, two years after the earthquake the area experienced several rainy weeks followed by a high intensity rainfall event. This event consisted of two peaks of several hours of rainfall, with intensities up to 33 and 31 millimeters per hour, and a total event duration of 15 hours. In total, 220 mm of rainfall fell in the two days surrounding the event.

360 During this event, a debris flow was generated by entrainment of loose landslide deposits, and the landslide dam located in the central channel was breached. Due to the dam breaching, the volume of the flow increased substantially, also due to more entrainment downstream. Upon leaving the Hongchun watershed, the debris flow material deposited in the Min River, with a thickness of up to 15 meters high and an estimated total volume of $7.11 \times 10^5 \ m^3$ (Tang et al., 2011). The Min River, which experienced a high discharge at this moment, was diverted laterally and flooded parts of the nearby newly reconstructed Yinxiu

365 town (Figure 6). For a more detailed description of the event, see also Tang et al. (2011) and Ouyang et al. (2015). A schematic overview of the event is provided in figure 5.
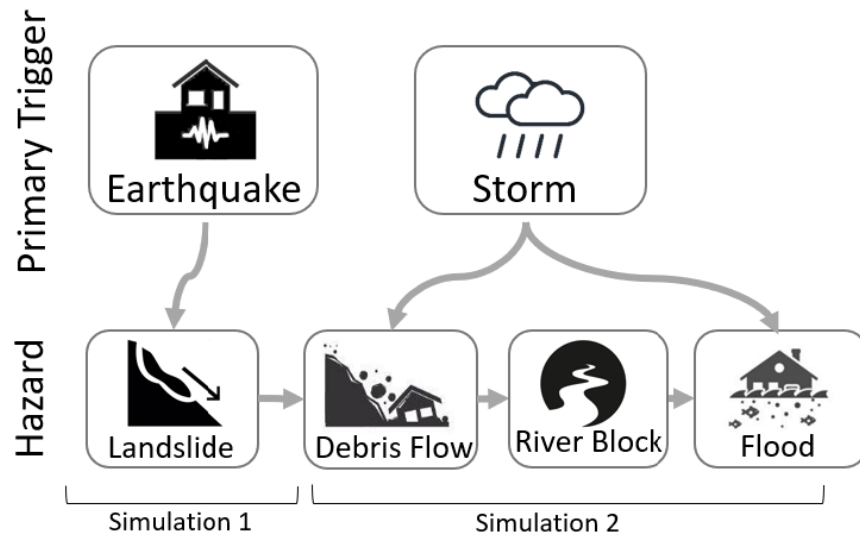
Figure 5 Top) A schematic overview of the stages of the described event. The events for simulation 1 occurred directly after the Earthquake in 2008. The events for simulation 2 after the rainfall event in 2010. Bottom) A view of the situation at the landslide dam in 2014 (as indicated in figure 4, photo taken from the south side of the main gully). From Mergili.at with permission from author.

In summary, the study area experienced two different multi-hazard chains that will be simulated.

- Co-seismic chain: The first one was experienced during the earthquake, when ground shaking and topographic amplification triggered a series of co-seismic landslides, some of which blocked the Hongchun stream;

- Post-earthquake chain: heavy rainfall triggered debris flows due to entrainment, which broke the co-seismic landslide dam. The resulting debris flow dammed the Min river, which was diverted into the town of Yingxiu.

All simulations include entrainment of estimated soil depth, hydrology and the related surface processes as described in the theory section.

3.2 Model Input and parameters

The input data is based on a combination of laboratory or field measurements and drone or satellite-based spatial data products (Table 1).

Table 1 List of input data and sources for the multi-stage multi-hazard modelling with OpenLISEM Hazard.

Spatial input parameters		
Base Map	Parameter	Source
Elevation	Pre-Earthquake DTM (z)	20m resolution elevation product from interpolated contourlines (unknown date)
	Post-Earthquake DTM (z)	Drone photogrammetry 2-meter surface elevation (filtered to DTM using PIX4D vegetation filter) (obtained fall 2018)
Land Surface	Land cover classes	Sentinel-2 classification at 10m resolution (trained spectral angle mapper)
	Mannings N (n)	Literature comparison with field photos
	NDVI	Landsat-8 images at 30 m resultion (2008) SPOT-4 product at 4m resolution (2010)

	Vegetation Cover	Estimated from NDVI using empirical method (Kalacska et al., 2004; Jiang et al., 2006)
	Root Cohesion (c_r)	Measured in field (12 samples) and extended based on land cover classes.
Soil Material	Texture (d_{50})	Measured from field samples (4 samples)
	Saturated Conductivity (k_{sat})	Measured from field samples (4 samples)
	Internal Friction Angle (ϕ)	Measured from field samples (16 samples) Literature values
	Cohesion (c)	Measured from field samples (16 samples)
	Porosity (θ_s), Matric Suction (ψ)	Literature Values derived from texture (Saxton et al., 2006)
	Density (ρ)	Measured from field samples (16 samples)
	Initial Moisture (θ_i)	Ground water model run for three months using GPM 30 minute interval satellite precipitation estimates.
	Soil Depth (h_s)	Soil depth modelling calibrated using landslide scarp depth (method from Ruette et al., 2013)
Shakemap	Peak Ground Acceleration (θ_s)	USGS shakemap (Wald et al., 2005)
Rainfall	Rainfall Intensities (R)	Rainfall station within Yinxiu provided high-accuracy hourly data. Additionally GPM 30-minute interval

		global rainfall product was used for pre-event ground water modelling.
Inventory	Landslide locations	Mapped from high-resolution imagery (Tang et al., 2017)

Global parameters

(besides multipliers for all spatial input data with default value of 1.0)

α	β	K	C	P	C_V
1	10	0.05	0.1	0.5	0.65

385 A pre-earthquake digital terrain model with 20 meters spatial resolution was obtained from the local government. Unfortunately, we were not able to obtain better quality pre-earthquake elevation data. Because of this a comparison of the pre-earthquake contour lines with post-earthquake elevation does not yield useful data. Post-earthquake surface elevation data were available at 2-meters spatial resolution, acquired from fixed-wing drone flights (See Figure 6) and filtered using the Pix4D DTM filter to remove vegetation (Pix4D, 2017). Flow simulations typically are most dependent on the accuracy and 390 spatial resolution of the elevation model. In order to have an effective compromise between detail and computation time, we resampled all input base maps to the final resolution of 10 meters, at which the simulations were carried out.

Pre-earthquake NDVI values were calculated at 30 meter resolution Landsat-8 images from 2008. A post-earthquake NDVI map was obtained from 4 meter spatial resolution SPOT-images acquired in 2009. NDVI values were used to estimate Leaf Area Index (LAI) by applying an empirical relation obtained from tropical forest data (Kalacska et al., 2004). We used it to 395 estimate fractional vegetation cover using a similar empirical relationships (Jiang et al., 2006).
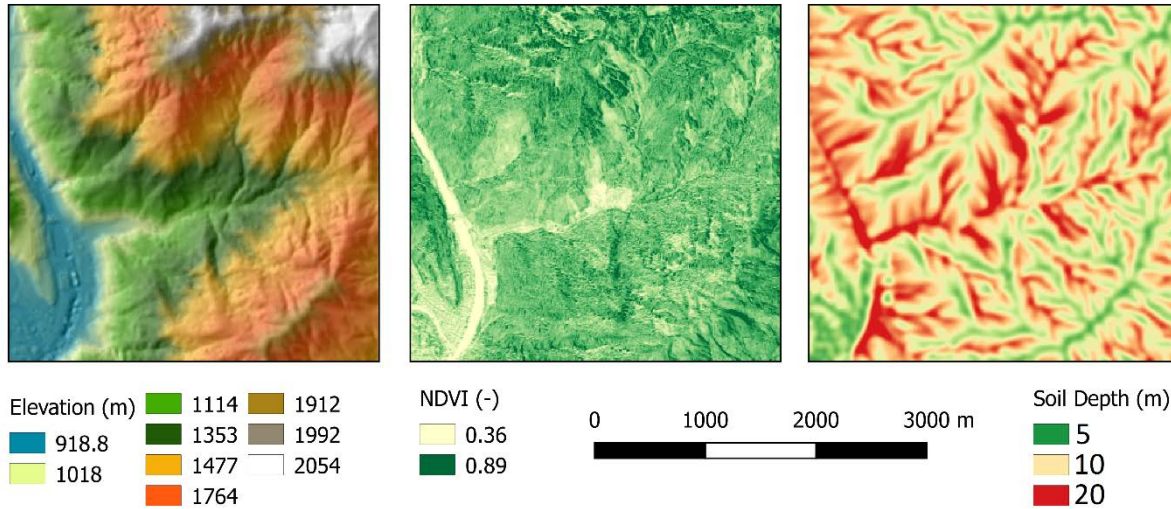
Figure 6 An overview of the input data for the first-stage simulation in Hongchun catchment: elevation model (left), NDVI (middle), modelled soil depth (right).

Spatial seismic acceleration data were obtained from the USGS ShakeMap product (Wald et al., 2005), developed using combinations of measurements and intensity prediction equations, and Peak Ground Acceleration (PGA) values were around 1.5 g for this earthquake in the Hongchun area. The PGA value reflects estimated surface shaking, but does not take into account the complex variability in site effects such as amplification due to soil or topography. Landslide material strength parameters were obtained from tri-axial strength tests performed for engineering reports ordered by the local government (Table 2; Yang, 2010; Hao et al., 2011; Li et al., 2011). The consolidated-drained triaxial tests were performed on samples acquired from both the deposition and source areas, although exact locations are unknown. The resulting average values for cohesion of 7.3 kPa and internal friction angle of 27 degrees were calculated from 16 samples. While the cohesion and density matches the values found in other studies (Ouyang et al., 2015; Domenech et al., 2019), the internal friction angle was estimated to be between 30 and 40 degrees in a previous study (Ouyang et al., 2015), based on measurements of internal friction angle on similar igneous rocks in the nearby Xiaojigou ravine. The difference between these values can be explained by the material used in the tri-axial tests. In our case, material from landslide depositional areas or areas close to a landslide source was used. These samples contain more fractured and loosened material. Thus, these measurements will provide a more appropriate value in post-earthquake entrainment simulations. The root cohesion is not used for slope stability in the model, as roots do not reach

24

the depth of the typical failure plane. Instead, the root cohesion is used to increase shear strength for the entrainment prediction. Here, vegetation cover influences the predicted erosion. However, for pre-earthquake slope stability estimations, a value of 35

415 degrees was used, as was done in other studies (Ouyang et al., 2015; Domenech et al., 2019). Textures were found to be clay-loam with large amounts of gravel. Saturated infiltration rates were measured in the field by using field ring infiltration tests. Because of the large amounts of gravel, and macro-pores within the materials structure, infiltration values were relatively high. Values were obtained for a total of four locations, which gave an average value of 65 mm/h for saturated conductivity. Other soil related parameter such as porosity, density and matric suction were obtained using the pedo-transfer functions from Saxton

420 et al. (2006).

Table 2 Strength parameters for the debris flow material in the Hongchun catchment (Yang, 2010; Hao et al., 2011; Li et al., 2011) and saturated hydraulic conductivity.

	Average (16 samples)
Cohesion (kPa)	7.3
Internal Friction angle (Degrees)	27.0
	Average (16 samples)
Density (kg/m3)	2145
Median Grain Size (mm)	3.1
	Average (4 samples)
Saturated Hydraulic Conductivity (mm/h)	65 mm/h

Soil depth values were obtained by applying the spatial soil depth model from Ruette et al. (2013), which uses steady-state assumptions to balance material production with soil movement according to an empirical formulation of erosion and lateral

425 transport. The production of weathered material depends on the weathering rate of bedrock. Since weathering rates are

generally difficult to obtain, this parameter becomes the main calibration parameter. Validation was done using soil depth

values obtained from landslide scarps. In this study, we used the pre-and post- earthquake elevation model differences provided

by Tang et al. (2019). From their data, we sampled elevation model differences in landslide source areas to obtain failure

depths, assuming that the failures were at least as deep as the top layer of weathered material. In case of shallow landslides,

430   we took the maximum landslide depth as soil depth. For the larger, deep-seated landslides, no samples were taken since it was

not possible to obtain a good estimate of the depth of the top layer. Additionally, we simulated a second layer within the slope

stability calculations with an additional depth of 20 meters to capture any deeper rotational slides within the bedrock material.

We assumed that this second layer did not contain groundwater, had an internal friction angle of 35 degrees, was subject to

sub-surface lateral forcing, and influenced by the weight of the upper layer. Calibration results and cumulative distributions of

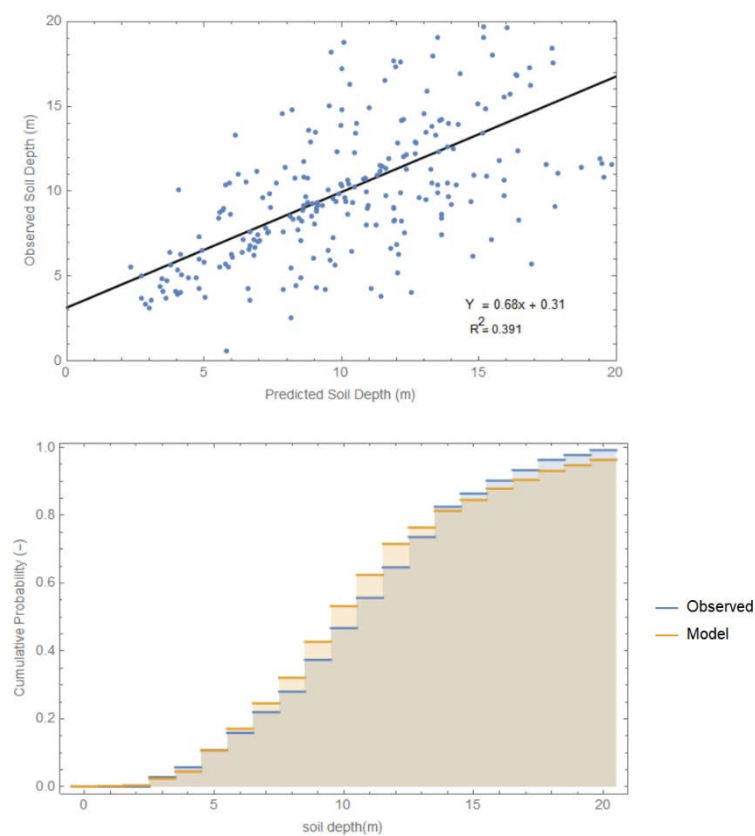435   depth values are shown in figure 7.

Figure 7 Soil depth simulation results. (Left) A comparison of predicted vs observed values. (Right) Probability distribution for observed and simulated soil depth values.

The effect of vegetation on slope stability and entrainment rates were taken into account by adding root cohesion. The recovery of vegetation in the landslide affected areas developed through distinct stages (Huang et al., 2015). We estimated the average root cohesion for the various vegetation classes using a combination of literature data and measurements (Schmidt et al., 2001; De Baets et al., 2008; Chock et al., 2015). We used the method as described by De Baets et al. (2008) which requires measuring root critical force and root diameters for all significant roots within a specific surface area. Then, after converting force to tensile strength, the total effect of the roots per unit area can be estimated using equation 40.

40
$$c_{root} = \frac{\sum T_i n_i a_i}{A}(\sin(\theta) + \cos(\theta)\tan(\phi))$$

Where c_{root} is the added apparent root cohesive strength (kPa), i is the root diameter class, T_i is the root tensile strength (kPa), n_i number of roots within the diameter class, a_i is the cross-sectional area of the root, A is the area of the soil occupied by roots (m2), θ is the angle of shear distortion in the shear zone (°) and ϕ is the internal friction angle (°). Note that term related to the shearing angle $(\sin(\theta) + \cos(\theta)\tan(\phi))$ is usually assumed to be approximately 1.2 (Baets et al.,2008). Here, we used a spatial calculation of this variable.

A total of 12 measurements of root cohesion averaged over a 0.1 m^2 area were done. On average, 108 roots were found per test site of 0.1 m^2, with an average diameter of 3.6 mm. Average values for young, post-landslide vegetation where found to be 4.8 kPa, averages for medium-sized vegetation where found to be 6.2 kPa. For mixed forest, literature values were used, and root cohesion was estimated to have a value of 8 kPa (Chock et al., 2015; Huang et al., 2015). For each land cover class, the root cohesion from the closest measured vegetation type was used. Finally, within each land cover class, we linearly scaled the root cohesion to fractional vegetation cover values that were derived from the NDVI both before and after the earthquake.

3.3 Calibration and Validation

The predicted co-seismic failure areas were calibrated using the landslide inventory and mapped deposition based on aerial imagery and pre-and post- event elevation data differences. Within the inventory, no separation between source and deposit areas was provided. Therefore we assumed that, based on field visits, on average the 25 % highest part of each landslide polygon reprented the source area. In order to compare the outputs of our model with others, we parameterized two other

regional slope stability models. The first of these is Scoops3D, which uses random spheroid sampling to find the landslides with the lowest- failure volumes, and lowest factors of safety for each pixel (Reid et al., 2015). This model can also use seismic shake maps as input. The second model is r.slope.stability, which uses random ellipsoid sampling to find the lowest factor of safety and failure depth for each pixel (Mergili et al., 2014). The version of the model that was used did not incorporate seismic acceleration, so the output is calibrated without addition of a seismic forcing. Recent developments of this software have added these effects. The Newmark displacement method (Newmark, 1965) was not used in our comparison. The primary reasons were the lack of predicted failure depths and the high similarity to the infinite slope model. When the critical acceleration is taken as threshold and failures occur when accelerations go beyond this value, results are identical to an infinite slope model that incorporates seismic acceleration. For both Scoops3D and r.slope.stability, the subsurface description is identical as to the input for OpenLISEM Hazard. As a measure of model fit, we used the Cohens Kappa value. This metric shows benefit over simple accuracy, especially for modelling landslide occurrence, since it compensates for the large amounts of true negative predictions (no landslide in model and inventory) that usually dominate landslide study sites (Bout et al., 2018).

The second phase of the modelling first simulates hydrology and a debris flow initiated by entrainment. Then, within the same simulation, the Min River is blocked by debris flow material, and Yinxiu town is flooded. Calibration for this part of the modelling is based on mapped deposition extent in the Min River, the flood extent in Yinxiu Town, and the estimated depositional volume (approximately $7.11 \times 10^5 \ m^3$).

Calibration of the entrainment and debris flow runout was based on the final spatial deposit extent at the catchment outlet. The calibration parameters for each part of the simulation are shown in table 3. An exception to this was the entrainment constant, for which no clear guideline was known to determine the value for specific terrain types. Based on earlier simulations and flume tests from Takahashi et al. (1992), a starting value was chosen of 0.05. For initial soil moisture content, the value is cut off at full saturation. Initially, each parameter was varied by choosing values between 60 and 140 percent of the original value. After initial calibration was done, the parameters were adjusted according to the steepest descent principle, in order to find the best set of parameter values. To have a level of validation in the simulations, the parameters resulting from calibration of the first chain were used as input for the second chain.

Table 3 Calibration parameters, their initial values and their final calibrated values for both chains.

Simulation Part	Calibration Parameters		
Co-Seismic Slope Failure	Soil Depth	Internal Friction Angle	Soil Cohesion
Original Average	4.5	27	7.3
Calibrated Multiplier	1.3	0.91	1.2
Hydrology, Flow and Entrainment	Entrainment Constant	Initial Soil Moisture Content	Manning's N
Original Average	0.005	80 %	0.127
Calibrated Multiplier	0.6	1.12	0.82

4 Results

Simulation results for the first chain, co-seismic slope failure and runout, are shown in figure 8 and 9. Both the accuracies and

490   Cohens Kappa values for each of the used slope stability models are shown in table 8.
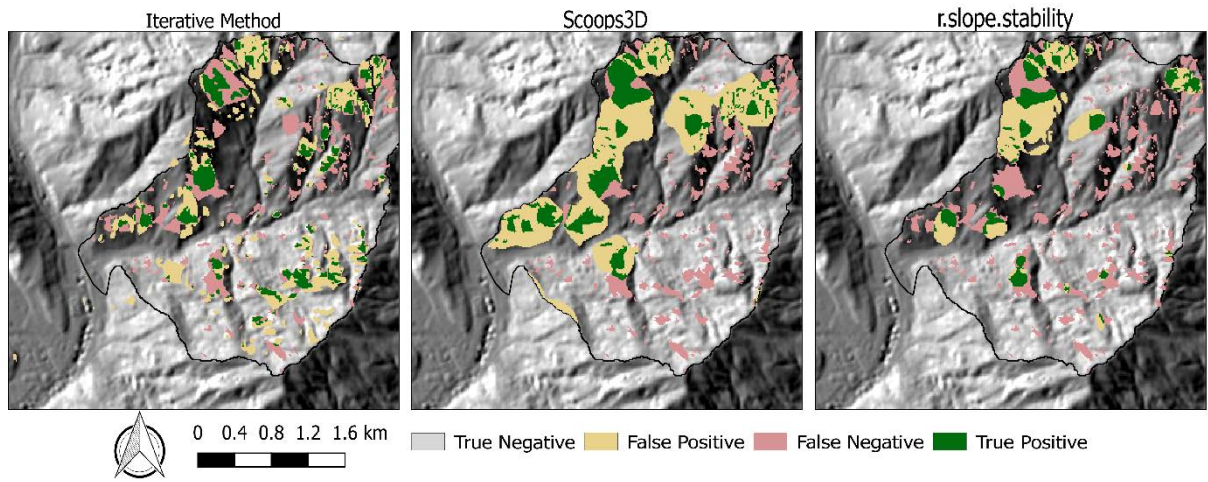
Figure 8 A comparison of simulated slope failure extent with mapped co-seismic slope failures. (Left) OpenLISEM Hazard Iterative Failure with sub-surface forcing, (Middle) Scoops3D random spheroid sampling. (Right) r.slope.stability random ellipsoid sampling.

29

Table 4 Slope stability simulation accuracy and Cohens Kappa values.

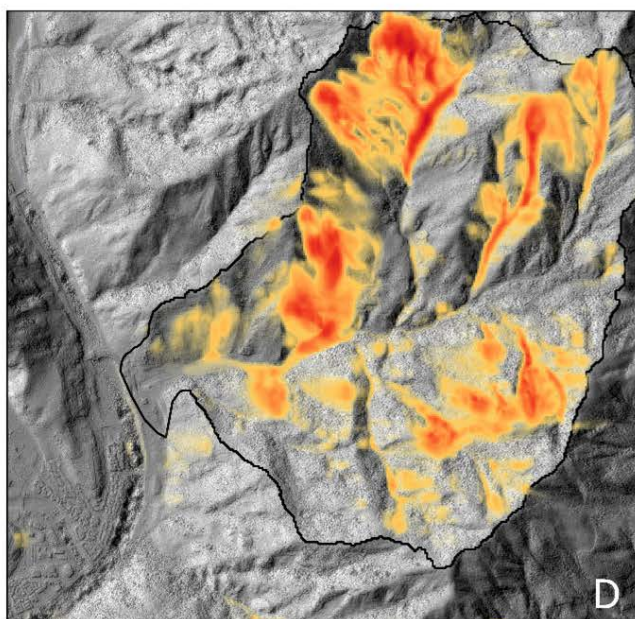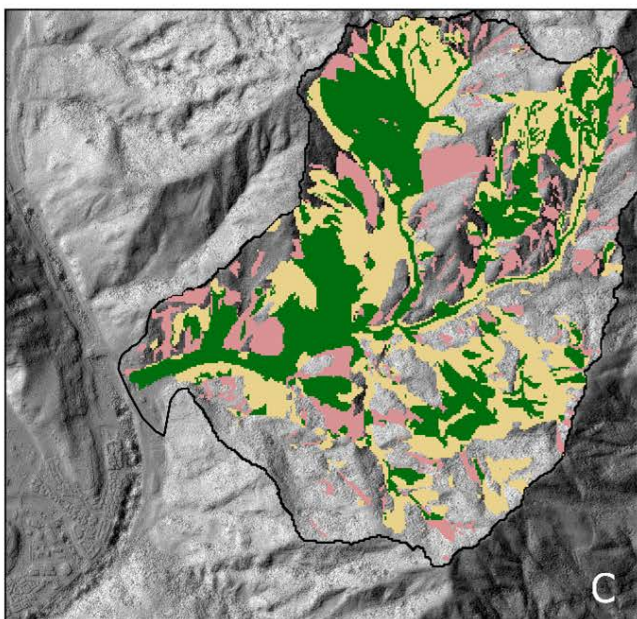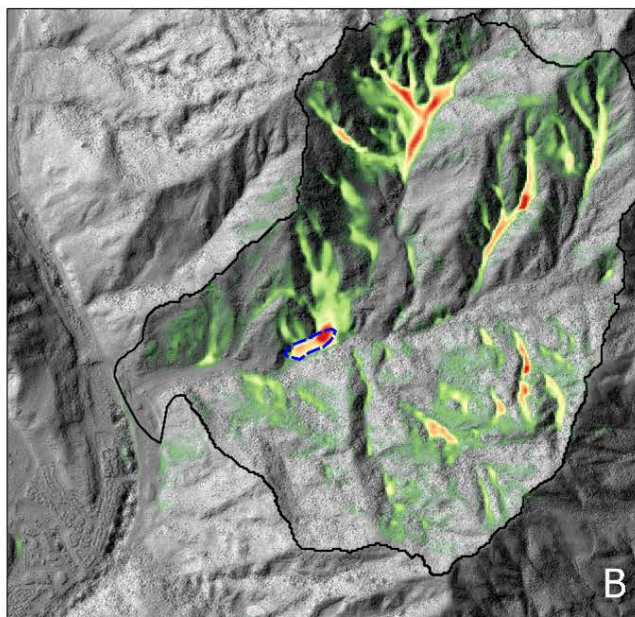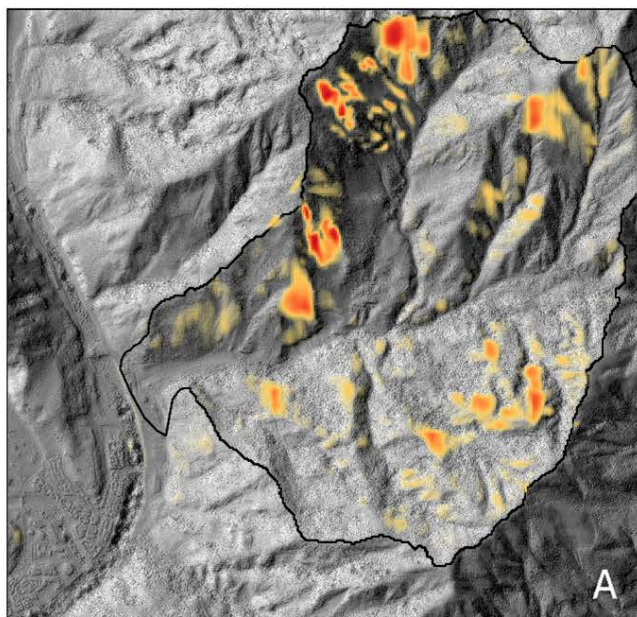| Model	OpenLISEM Hazard	Scoops3D	r.slope.stability	Mapped
True Negative (m^2)	3775700	3420700	3971800	4258397
False Positive (m^2)	530100	476100	627800	0
False Negative (m^2)	587300	939300	391200	0
True Positive (m^2)	315400	369400	217700	950103
Accuracy	79	72	81	100
Cohens Kappa	0.232	0.181	0.190	1
Average Size (m^2)	36394	140253	94028	21547

495

The general spatial patterns are predicted reasonably by all models, but the models differ considerably in details. For the ellipsoid and spheroid sampling done by r.slope.stability and Scoops3D, the failures are larger than those actually mapped (Table 4). For the iterative method, sizes are mixed but much more similar. Major landslides, in particular in the north, are predicted with similar size, although not on the exact location, by all models. The highest accuracy (81 %) is obtained using

500 r.slope.stability, and the highest Cohens Kappa (0.232) value with OpenLISEM Hazard. The OpenLISEM Hazard iterative method shows the best reproduction of the general pattern, in particular since both Scoops3D and r.slope.stability lack slope failures in the southern half of the catchment. Of the three models, r.slope.stabiltiy and OpenLISEM Hazard show similarity in total failure area when compared to the inventory. Despite the achievements of the model, errors remain large, and the Cohens Kappa values indicate all models have low to moderate reliability.

505

4.1 Runout and the blocking of the Hongchun stream

When slope failures are simulated, OpenLISEM Hazard automatically introduces landslide runout by transferring the failed volume and its properties to the Mohr-Coulomb solid-fluid mixture flow equations. The depth of slope failures determine directly the amount of solids and fluids introduced (Figure 9D). The landslide material moved down the slopes into the main

channel of the Hongchun watershed, blocking it in at least one location (Figure 9A). The accuracy for the calibrated simulation was 64 percent with a Cohens Kappa value of 0.28 (Table 5), which is mainly be attributed to the accuracy of the failures that started this process (Figure 9B). Runout distances are similar to those mapped, indicated by the landslides reaching the main channels within the Hongchun catchment, but not reaching the Min river. In one location the channel was blocked by a deposit of 12 to 18 meter deep which was simulated with high accuracy as compared to the mapped blockage (Figure 9B). Engineering reports indicate a similar depth (16 meter) for the landslide dam (Yang et al., 2010; Hao et al., 2011; Li et al., 2011). We considered to use the landslide initiation polygons from the inventory to increase the accuracy of the runout simulation. However, since the aim of this research is to provide a true multi-stage modelling setup, we used the integrated prediction of slope failures as input in the runout modelling.

Failure Depth (m)
- 0
- 10
- 15
- 20
- 30

Comparison
- True Negative
- False Positive
- False Negative
- True Positive

Mapped Landslide Dam

Deposit Depth (m)
- 0
- 4.5
- 9
- 13.5
- 18

Maximum Flow Depth (m)
- 0
- 10
- 15
- 20
- 30

0 0.4 0.8 1.2 1.6 km
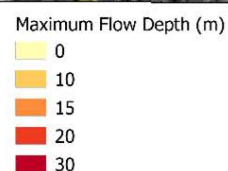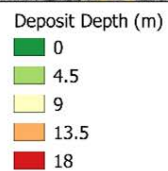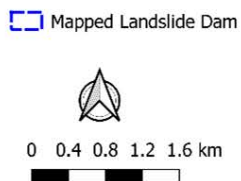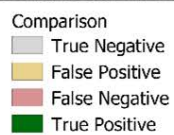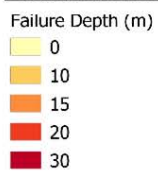
520 **Figure 9 (A) Initiation depth from the slope failure simulation. (B) The simulated final deposit depth of the landslides. Blockage location shown with blue outline (Mapped Landslide Dam) (C) A comparison of modelled landslide runout with the mapped landslide inventory. (D) Maximum landslide runout flow depth.**

Table 5. Confusion matrix for the landslide runout prediction in Hongchun watershed.

Model	Runout (m^2)	525
True Negative	2092900	
False Positive	1260500	
False Negative	613900	
True Positive	1241200	
Accuracy	64	
Cohens Kappa	0.28	

4.2 Validation of failure and runout for the major central landslide using elevation model differences

Two large landslides occurred in the northern part of Hongchun catchment. One of those, near the center of the area, blocked the main channel of the catchment. For this landslide, pre- and post-earthquake elevation models from LiDAR data are

530 available (Tang et al., 2019), which were used to calculate the landslide volume. For this particular area, we compared the predicted elevation model differences based on slope failure and deposition from our modelling chain with the results from the LIDAR DEMs (Figure 10).
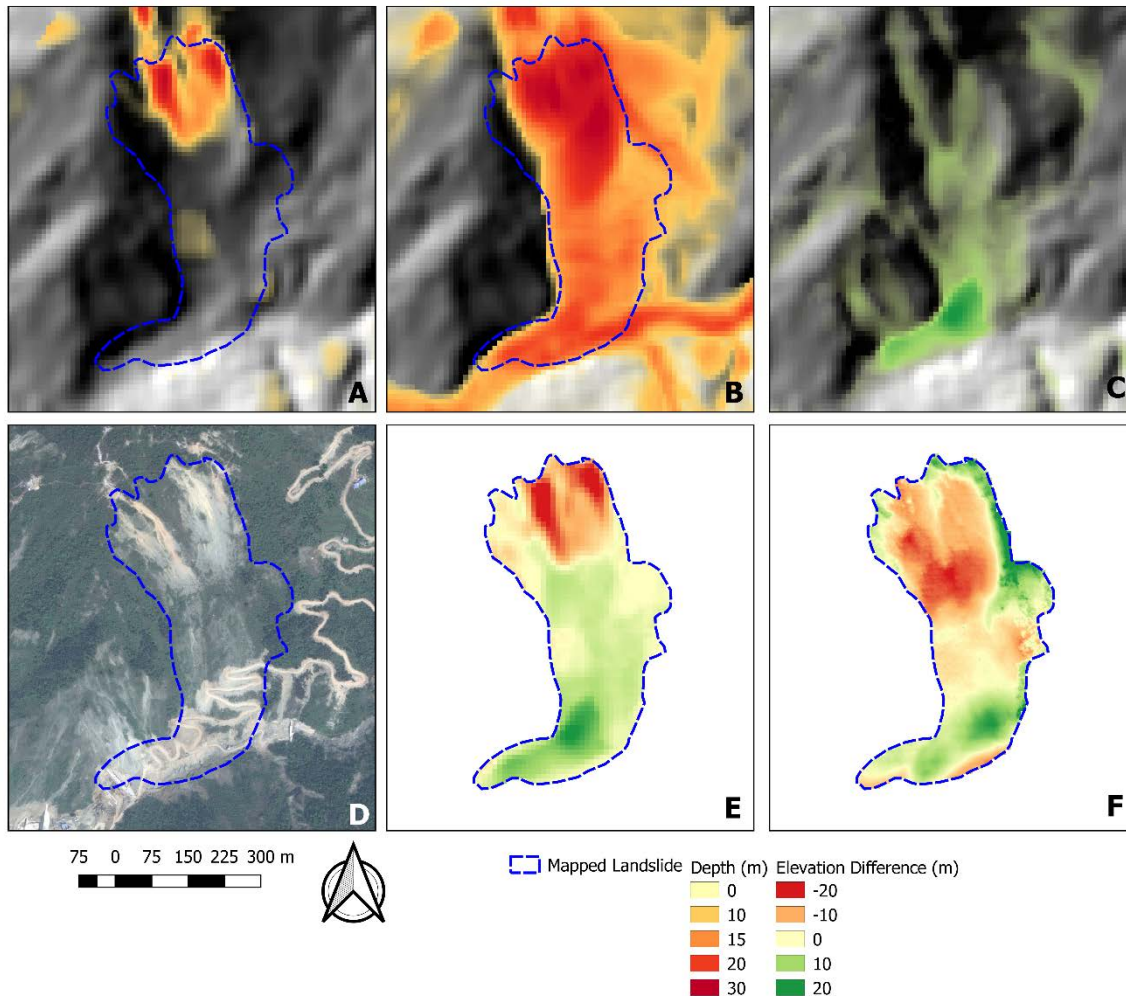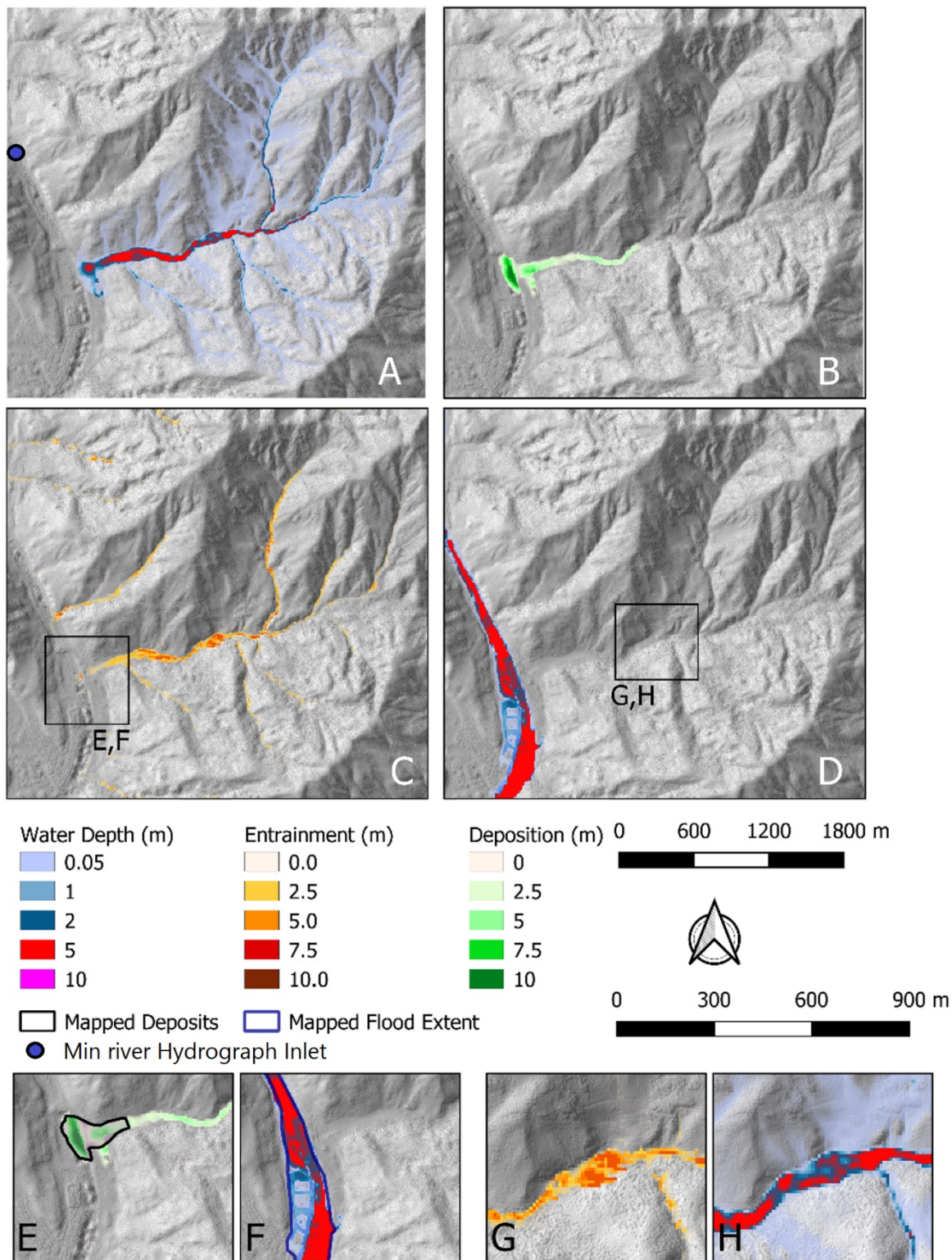
Figure 10 An overview of the central largest landslide in the Hongchun watershed. (A) The simulated failure depth, (B) The simulated maximum runout depth, (C) The simulated deposition depth, (D) Post-Earthquake satellite image (Worldview, 2011) Note the mining activities in the landslide deposit area (E) Predicted elevation model differences due to co-seismic landslides. (F) Observed elevation model differences from pre-and post-earthquake LiDAR data.

Both the slope failure and runout thicknesses are predicted with high accuracy for this landslide. The landslide deposits of around 20 meters thick remained in the main channel without spreading significantly. These deposits have later been mined as materials for local construction. As can be seen in Figure 10 the failure, deposition and elevation differences are highly similar with matching spatial patterns.

34

4.3 Simulation of the second multi-hazard chain

The results from the modelling of the second stage show a full physically-based simulation that reproduces the behavior and the impact of the event (Figure 11). This rainfall event with two distinct peaks resulted in a rainfall amount of 220 mm in two days, which was modelled in time steps of 0.5 seconds. Due to the large rainfall volume, runoff increased rapidly leading to large amounts of sediments that were entrained from the co-seismic landslide deposits. Within the simulation, entrainment takes place after runoff has converted into streams. There, higher water pressures and velocities provide shear stress on the surface that is sufficient to overcome the materials internal stability. Near the outlet of the watershed, entrainment decreased due to a decrease in slope steepness. This decreased flow velocities, but also increased internal stability of the available material. Because of this, entrainment stopped, the flowing material lost momentum and was finally deposited in the Min River.

Water Depth (m)
- 0.05
- 1
- 2
- 5
- 10

Entrainment (m)
- 0.0
- 2.5
- 5.0
- 7.5
- 10.0

Deposition (m)
- 0
- 2.5
- 5
- 7.5
- 10

0   600   1200   1800 m

0   300   600   900 m

Mapped Deposits   Mapped Flood Extent

Min river Hydrograph Inlet

555 **Figure 11 Calibrated simulation results for the second chain in the Hongchun watershed. (A) Maximum total flow depth; (B) Final deposit depth; (C) Entrainment depth; (D) River flood depth; (E & F): Zoom of Hongchun outlet with (E): Deposition depth compared with mapped extent, (F) River flood depth compared to mapped flood extent; (G &H) Zoom of Hongchun Landslide Dam with (G) Entrainment depth and (H)Maximum flow depth.**

Table 6 Confusion matrix, accuracy and Cohens Kappa values for the debris flow deposition and flooding of the Min River.

Model aspect	Deposition	Flood
True Negative (m^2)	516000	331543
False Positive (m^2)	28000	34510
False Negative (m^2)	35000	51890
True Positive (m^2)	213000	546132
Accuracy	92	91
Cohens Kappa	0.84	0.81

560

The simulated debris flow reaches the Min River and the deposits accumulate in the river. Most of the momentum has been lost before the material leaves the Hongchun watershed, and even though the Min River has a velocity of 7 m/s the deposited volume is too large to be eroded by the Min river. Both the total deposit volume in the river, and the extend of the deposits compare well to the measured and mapped values. The deposits were modelled with an accuracy of 92 % and a Cohens Kappa

565 value of 0.84 (Table 6). The modelled deposited volume is $5.82 \times 10^5 \ m^3$ (the observed estimation of the deposited volume is $7.11 \times 10^5 \ m^3$)

As a final stage of the event, the model predicted the flood behavior in the town of Yinxiu by the Min River, as its main course was blocked by the debris flow deposits. The modelled damming area correlates well with the observed deposit volumes and flood extents, obtained from the interpretation of aerial images and field photos from the event (Figure 14). The flood accuracy

570 is 91 % with a Cohens Kappa value of 0.81 (Table 6). Since the elevation data was up scaled from 2 meters resolution to 10

meters, the multi-story buildings merged with small streets to become a joined obstacle for the flow, which corresponds to the visual observations.

While validation using comparison to mapped extent is a useful tool, it does not guarantee all aspects of the hazard are correctly simulated (e.g. timing, velocities, heights). While a model might have correctly predicted the extent of impact, it might predict

575   the occurrence to early or late, with wrong velocities or flow heights. While we do not have data on flow heights on velocities, we confirmed with local authorities the debris flow was reported at 03:30 hours. In our simulation, the first peak of solid material at the outlet occurs at this time (figure 12). The major peak of debris material occurs later, at 06:00, but we could not confirm in Yinxiu town for how long the debris kept arriving at the Min river.
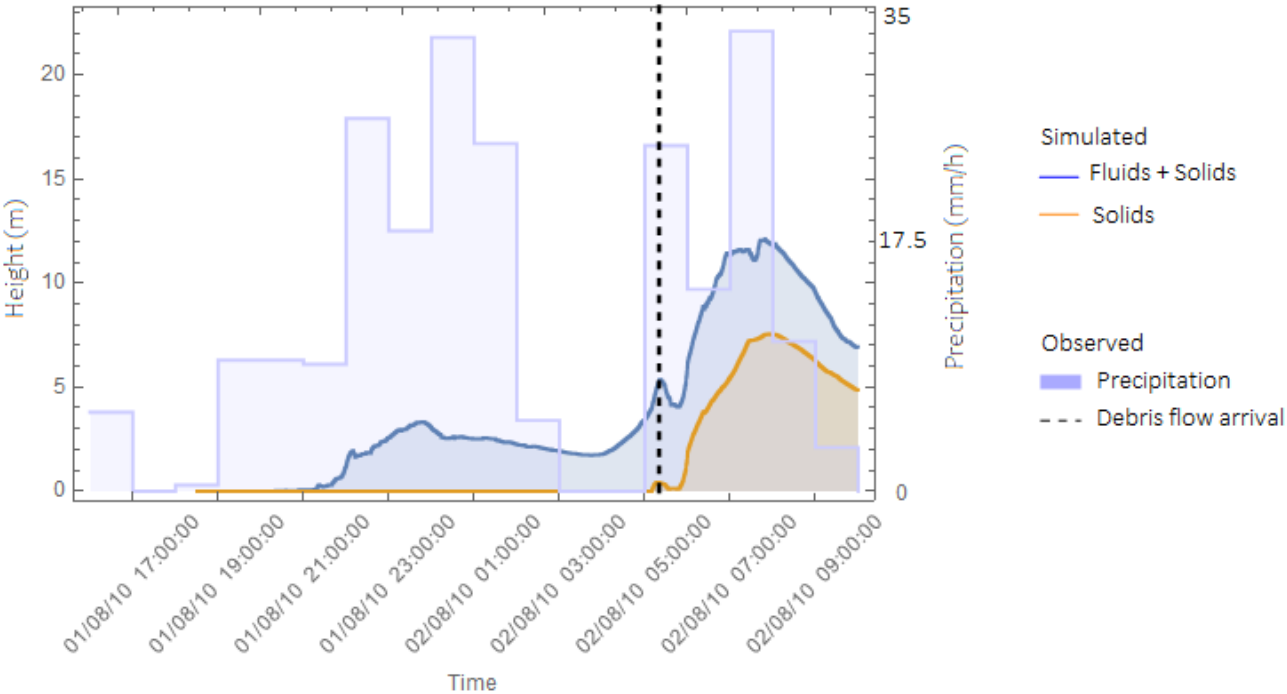

580   *Figure 12Time series data for rainfall, total flow height and solid flow height at the Hongchun outlet. Reported debris flow occurrence time is indicated as 'debris flow'.*

5   Discussion

5.1 Uncertainties in modeling the multi-hazard chains

585 Several major obstacles in the simulation of co-seismic landslide occurrence can be identified, which are related to the assumptions and techniques used in the models . The iterative method that is implemented in OpenLISEM Hazard, assumes that, at least initially, failure surfaces are parallel to the terrain surface. This assumption can lead to a variety of issues when the terrain has small-scale variations that do not represent the overall topography. This assumption is not present in the random ellipsoid sampling methods. The iterative method shows similar failure depths and locations, but generally separates slope

590 failures more, where the other models show larger joined failures. The predominant cause of this behavior most likely lies in the sub-surface force iteration, where the potential failure surface is also initially assumed parallel to the surface. Then, when an obstacle exists that alters slope around several pixels, the sub-surface forces are blocked, and potentially larger failures become disconnected (Figure 13).
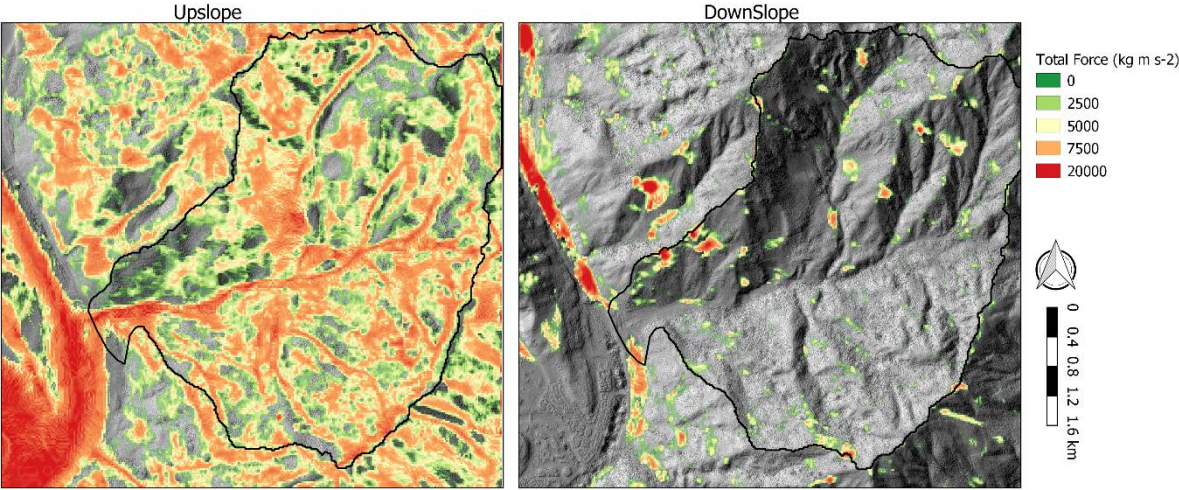
595 *Figure 13 The upslope (left) and downslope (right) additional forcing that is estimated based on an iterative solution for sub-surface force redistribution.*

Secondly, structural geological input data are not available, and cannot be used in the iterative method. For three-dimensional analysis using random ellipsoid sampling, structural weaknesses could be implemented by altering strength properties of specific layers. When such data are available, applications of the detailed random ellipsoid sampling method, can allow for a

600 greater predictive value (Mergili et al., 2014; Cance et al., 2017; Tun et al., 2018).

Furthermore, seismic acceleration of material is a complex and dynamic process, driven by seismic waves compressing and stretching the sloping materials. Such waves reflect and refract based on material properties and boundary conditions, which leads to a variety of topography or material-based amplifications. These amplifications are generally important in landslide hazard modelling (Jafarzadeh et al., 2015). However, shake maps produced by the USGS utilize empirical predictive functions to spatially extend ground accelerations, and ignore these crucial local amplification effects. As a result there is high spatial uncertainty in the peak ground acceleration values we have used as input. Such uncertainties can be overcome by linking slope stability approaches to seismic wave modelling, a computationally heavy task that has of yet not been performed for the Wenchuan earthquake.

The final calibrated values of the input parameters were within a reasonable range (between 50 and 150 percent) with respect to the original estimated ones. Two parameters stood out significantly in the calibration process. The first of these, soil depth is a crucial parameter, as it determines the amount of material that is released, which is of direct influence in the runout modelling. This can indirectly influence the amount of material available for entrainment by flow at a later stage. In an active landscape, soil depth patterns are determined by rock weathering rates and mass transport/wasting. Soil depth increases until there is sufficient material to induce slope failures or significant erosion. As a result, at many locations, combinations of soil depth and slope can be near a critical state. The spatial component of soil depth is therefore of high importance. Despite its importance, soil depth is very difficult to measure over larger areas, and has a high uncertainty in most model applications (Kuriakose et al., 2009). Because information on soil depth is difficult to obtain through direct observation or remote sensing, it is generally obtained through modelling approaches (Kuriakose et al., 2009; Ruette et al., 2013). Another reason for the uncertainty in soil depth information is that a soil layer is a theoretical concept that does not always translate well into reality, where weathering is a more gradual process. A second variable which was difficult to estimate is the entrainment coefficient. Currently, there are several types of entrainment equations available in the literature, but most of these lack significant guidelines for selecting practical entrainment parameters (Iverson and Ouyang, 2015). Besides this coefficient, other parameters used in the entrainment equations, such as soil cohesion, internal friction angle and moisture content were measured in the laboratory and are common values for geotechnical research. However, the number of samples that are tested for these geotechnical parameters are always limited, and their spatial variability is generally high.

5.2 Ensemble Simulations

To analyze the uncertainties within the multi-hazard multi-stage modelling setup, we extended the calibration process to an ensemble analysis. In total, for each of the 6 calibration parameters, 3 equal-interval values were used (calibrated values, and the values plus or minus a given range of 10 – 50 %, as indicated in table 7. Thus, the first simulation was repeated 27 times. The best estimate was used as input for the second simulation, which was similarly repeated 27 times. In total, 56 simulations were thus performed, out of which normalized frequencies were generated for hazard occurrence. We defined a threshold of 0.25 meters above which a flow is counted as an actual hazard occurrence to avoid that the results would include runoff with insignificant depths.

Table 7 Parameter settings for the ensemble simulations.

Co-Seismic Slope Failure	Soil Depth (m)	Internal Friction Angle (radians)	Soil Cohesion (kPa)
Calibrated Value (average)	5.85	24.57	8.8
Variation range (+/- %)	30 %	30 %	30 %
Hydrology, Flow and Entrainment	Entrainment Constant	Initial Soil Moisture Content	Manning's N
Calibrated Value (average)	0.003	89%	0.10
Variation range (+/- %)	50 %	10 %	20 %

41

Figure 14 shows an ensemble plot for each stage of the simulation. For each location, these maps show the normalized probability of hazard occurrence within the ensemble of simulations.
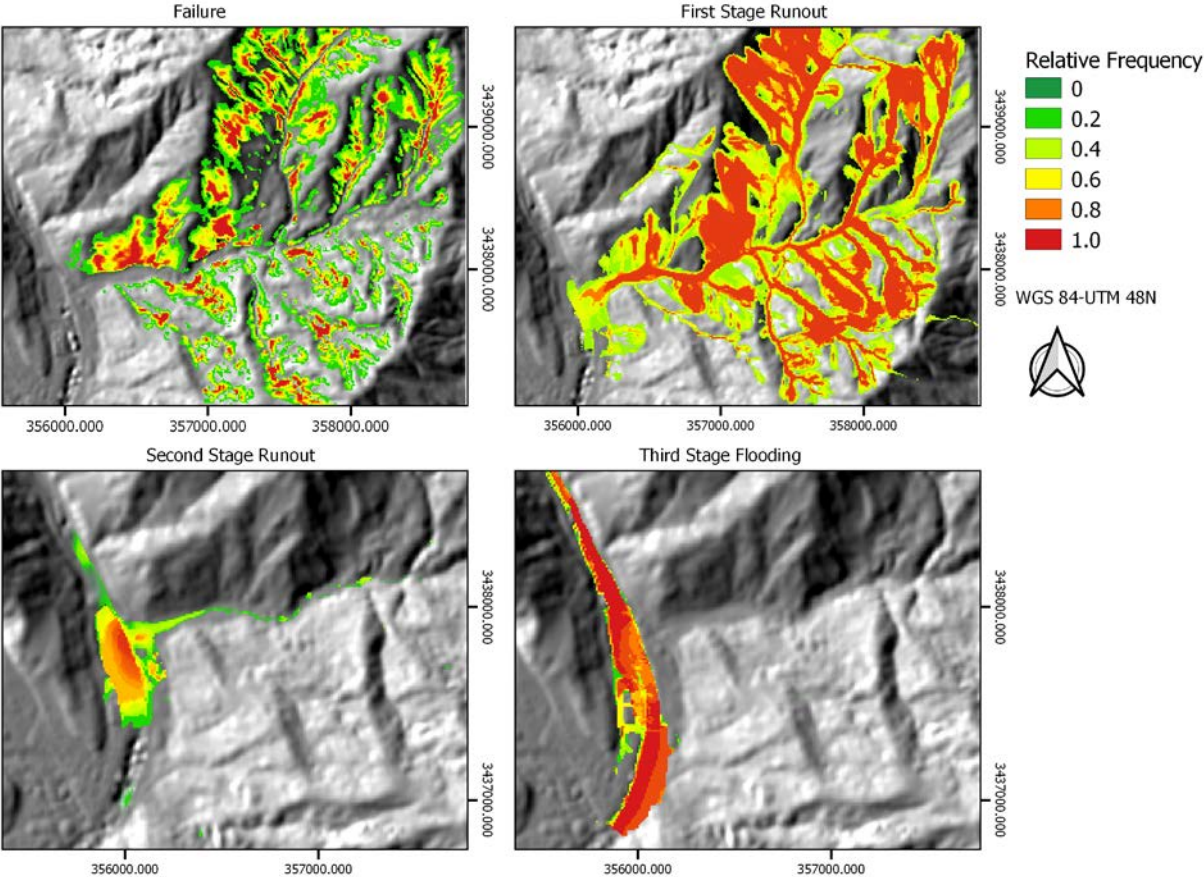

Figure 14 Ensemble simulation results for the Hongchun watershed. Visualized is the normalized probability, based on the
640 *ensemble of runs with varying input parameters, of the hazard occurring at each location. (A) Co-seismic slope failure. (B) co-seismic landslide runout. (C) Post-seismic debris flow deposition. (D) Post-seismic river flooding due to blockage.*

The four maps in Figure 14 illustrate how much the variation of the input parameters influences the simulated hazard for the four stages of the multi-hazard chain. The prediction of co-seismic slope failures shows the highest spread, and therefore the highest influence on the total event variability. The uncertainty in the input parameters influences the slope failure equations
645 most, since we have simulated the multi-stage event as an integrated sequence where the uncertainties in one process influence various other processes. Despite the uncertainties, there is a substantial certainty that flooding of Yinxiu town will occur,

independent of the input parameters. For all performed simulations, the deposition volume in the Min river is never below approximately a third ($2.1 \times 10^5 \, m^3$) of the estimated volume ($7.11 \times 10^5 \, m^3$). For at least 80 percent of the simulations, there is at least some flooding experienced with a depth above 50 centimeters in Yinxiu. In comparison to other multi-stage

650   hazard studies, these numbers are relatively high (Mergili et al., 2018b). Mergili et al. (2018b) reported that threshold behavior and non-linear effects dominated the alterations in model behavior with changing parameters. While the event they describe is quite different from the Hongchun disaster, there is a similar influence from threshold effects to the interpretation and certainty of model outcomes. In this current study, threshold effects most likely exist related to the landslide dam behavior in both the Hongchun watershed and the Min river. With altered input, there could be insufficient material for landslide dam creation, or

655   not enough flow and entrainment for breaching. However, we do not encounter scenarios that fall below the threshold of breaching in our ensemble.

There are several factors that drive the high likelihood of flooding in Yinxiu town. The event is initiated by several triggering conditions, or *forcings*, such as the seismic acceleration and rainfall, which occur in a very steep watershed, which determine the behavior of the hazardous processes. Seismic accelerations during the 2008 earthquake reached the 10th and highest USGS

660   category for seismic acceleration (>139% g). Similarly, the 2010 rainfall event resulted in 220 mm of accumulated rainfall within 48 hours, with significant rainfall in the weeks before. For events with a smaller return period, and smaller intensity of the triggering process, variability and uncertainty in the potential outcomes might be larger. An example is the occurrence of landslides long duration by low intensity rainfall, is a much larger challenge for physically-based modelling (van Beek, 2002). In our case, material strength parameters must deviate significantly from their measured and estimated values in order not to

665   result in slope failure under such extreme seismic acceleration. Thus, the severity of the triggering events causes the simulations to predominantly show major slope failures, debris flows, deposition in the Min river and finally flooding of Yinxiu town.

5.3 Usability

A major challenge for the application of such type of multi-hazard modelling is the step from back-analyzing past events to forward prediction of future events. In the case of back-analysis, calibration is possible on data from the event itself, whereas

670   predicting future events must be done without knowledge of the hazard that will occur. By calibrating on data of multiple events, and validating on other events (checking for accuracy using calibrated input from other events), a more robust model

can be established. When validated on similar events, a higher level of confidence can be generated in the abilities of the model to predict future events. In the case of the Hongchun watershed, the accuracy of the presented numerical experiments depended on thorough calibration. This is caused by several factors, such as the uncertainties in the input data and the limited accuracy

675 of the assumptions made within the model equations. In studies where multi-stage multi-hazard events are considered, this becomes even more difficult due to threshold effects and stacking uncertainties (Mergili et al., 2018a). Despite these issues, calibration is possible by performing model runs with a large set of varying input parameters and comparing the output with measured data on the event (e.g. discharge, extent of landslides, debris flows or floods). Validation options, on the other hand, may be very limited as similar events are very rare. Debris flows occur more frequently within the watershed and can therefore

680 be both calibrated and validated (Domenech et al., 2019). However, the multi-hazard chain as described in this research is a rater unique sequence of events that does not easily allow for validation, except when looking at individual components. Even then the co-seismic slope failure and runout stages do not occur frequently within the same region. Thus, we run into two primary issues in the predictive use of multi-stage and multi-hazard modelling. Firstly, the complex modelling has internal uncertainties that propagate, stack and provide a challenge in calibration. Secondly, such events occur with very low frequency

685 (Kappes et al., 2012), and can therefore rarely be further calibrated and validated. Despite the difficulties in the calibration and validation process for multi-hazard multi-stage modelling, we have shown that for the Hongchun watershed, many aspects of the first sequence had a high likelihood despite the uncertainties. This indicates the possible use in predicting future events, especially when ensemble analysis is performed to show the relative spread of model results. However, this is computationally intensive, and cannot be carried out over large areas yet.

690

6 Conclusions

We have investigated the potential for understanding and predicting complex multi-hazard co-seismic process chains A physically-based model is used that allows for the simulation of multi-stage and multi-hazard chain events in mountainous terrain. Catchment-based hydrology was combined with slope stability analysis under seismic acceleration. Entrainment of

695 loose material was implemented to alter both topography and the composition of the flow. The modelling setup is able to fully

simulate the behavior and impact of multi-stage and multi-hazard events. The developed model code is available as part of the on-going development of the open-source OpenLISEM Hazard model (www.lisemmodel.com).

The model was tested in the Hongchun watershed, located near the epicenter of the 2008 Wenchuan earthquake, in two sequences of hazard interactions. The first sequences was the generation of earthquake induced landslides, that resulted in

700   runout of landslide materials and the blockage of a stream channel. The second sequence was the triggering of debris flows by extreme rainfall, resulting in the breaking of the existing landslide dam, and the formation of a debris flow fan in the main river, forcing the river to flood the city on its banks. The modelled slope failures show a reasonable accuracy when compared with the actual landslide inventory. The failure simulation is the least accurate process within the simulation (accuracy 64 %). Improvements in this process might be possible using a higher quality ground shaking input map that includes topographic

705   amplification and other non-linear terrain-induced effects. Furthermore, a better spatial estimate of the sub-surface structure and the three-dimensional variability of strength parameters could improve the accuracy. However, current techniques for simulation of regional failure volumes are still often not achieving desires accuracy (Wasowski et al., 2011). Over time , such type of modelling should be able to translate the modelling of seismic acceleration for many earthquake scenarios, into a probabilistic earthquake-induced landslide hazard map.

710   The runout of the co-seismic landslides and the debris flow that was triggered two years later was predicted with high accuracy. Pre- and post- earthquake elevation model differences were used to validate the modelling outcomes spatially for the largest central landslide, where high accuracy elevations models were available for both pre- and post-earthquake periods. In particular, the blocking of the Hongchun stream by co-seismic landslide runout was simulated with good agreement (accuracy 91 %). During the simulation of the 2010 rainfall event, a debris flow was initiated by entrainment, and the landslide dam was

715   breached. Eventually, the model simulated with relatively high accuracy the flood behavior in the second stage of the event (accuracy 92 %).

The sensitivity of the model was further analyzed by looking at ensemble simulation results. Uncertainty propagated through the different stages of the simulations. Despite this uncertainty, the ensemble models showed a high likelihood of flooding in Yinxiu. The model results show high certainty due to both the magnitude of the seismic accelerations, rainfall intensities, and

720   the equations guiding the gravitational flows. This does not mean that the model is able to predict future event with equal

reliability. However, it does indicate that, when the inherent uncertainties are taken into account, predictions from advanced spatially distributed and physically-based models can provide insight and have some predictive value. Simulation results should be treated with caution. However, with validation and advancements in the understanding of the physical processes, multi-stage multi-hazard modelling might become a useful and trusted tool for decision makers in multi-hazard risk

725 assessment.

Author Contributions

All authors contributed significantly to this final works. C. Tang and C. X. Tang carried out field works and laboratory test fort he model, as well as helped develop the model theory. V. Jetten and C. van Westen provided assistance to the hydrological modelling, interpretation/discussion of results as well as writing. B. van den Bout developed the model code, carried out the

735 simulations, and wrote the methodology.

Code availability

The LISEM model, which was used in this research, is an open-source multi-hazard modelling tools. The software and source code are available from www.lisemmodel.com, together with documentation and example datasets. The source is written in c++ and compiles on windows and linux based operating systems. Visit the github repository to get started

740 (https://github.com/bastianvandenbout/LISEM)

Data availability

A dataset for Hongchun Gully, which was studied in this work, is provided on the LISEM website (www.lisemmodel.com). For more information on how to download and use this datasets, visit the downloads page.

Parameter List

745 $|\vec{u}|_{cr}$ is the critical velocity for deposition ($m\ s^{-1}$)

$\overrightarrow{F_{lat}}$ is the vector of laterally acting forces ($kg\ m\ s^{-2}$)

h_s is the depth of the failure plane (m)

S_f is the surface friction term (-)

S_f the momentum source term ($m\ s^{-2}$)

750 U_T is the settling (or terminal) velocity of a solid grain ($m\ s^{-1}$)

U_T the settling velocity ($m\ s^{-1}$)

z_0 is the lowest neighboring elevation (m)

α_s is the volumetric solid content of the flow (-)

ρ_f is the density of the fluid ($kg\ m^{-3}$)

755 ρ_s is the density of the solids ($kg\ m^{-3}$)

τ_c is the critical shear stress (Pa)

$C_1 = c$, $C_2 = (((\gamma - m\gamma_w)z + m\gamma_w z)$, $C_3 = ((\gamma - m\gamma_w)z)$ are simplifying compound parameters (-)

K_s is the saturated conductivity ($m\ s^{-1}$)

$\vec{S}$ is the normalized slope vector (-)

760 T_i is the root tensile strength (MPa)

V_d is the darcy flow velocity ($m\ s^{-1}$)

a_i is the cross-sectional area of the root

c' is the effective cohesion of the soil (kPa)

c^b is the cohesion of the bed material (Pa)

765 c_{root} is the added apparent root cohesive strength (kPa)

d_{50} is the median grain size (m)

f_{pot} is the potential infiltration rate ($m\ s^{-1}$)

n_i number of roots within the diameter class

n_{td} is the turbulent dispersive coefficient ($m^{\frac{1}{2}}s^{-1}$)

770   u_b is the basal velocity ($m\ s^{-1}$)

α^b is the volumetric solid concentration of the bed material (-)

α_{eq} is the equilibrium volumetric solid concentration (-)

γ_w is the density of water ($kg\ m^{-3}$)

θ_i is the initial soil moisture content ($m^3\ m^{-3}$)

775   θ_s is the porosity ($m^3\ m^{-3}$)

ρ_{eff} is the total effective density of the flow ($kg\ m^3$)

τ_y is the yield stress (Pa)

D is the deposition rate ($m\ s^{-1}$)

d is the grain diameter (m)

780   d is the median grain diameter (-)

D the force demand (denominator of equation 3)

E Is the rate of change of the basal topography (erosion rate) (ms^{-1})

F and G are the scalar functions describing the flow velocity of solids and fluids respectively (-)

g the gravitational acceleration ($m\ s^{-2}$)

785   h being the flow height (m)

h is the hydraulic head (m)

I the infiltration (m)

M is an empirical parameter depending on the Reynolds number (≈ 0.2) (-).

n is the Manning's n friction coefficient ($s\ m^{-\frac{1}{3}}$).

790   R is the rainfall (m)

Re is the particle Reynolds number (-)

S is the friction term ($m\ s^{-2}$)

u is the flow velocity ($m\ s^{-1}$)

α is the first viscosity parameter (-)

795 β is the second viscosity parameter (-)

η is the dynamic viscosity of the fluid ()

τ is the shear stress (Pa)

A is the area of the soil occupied by roots (m^2)

A is the mobility of the interface (-)

800 C is the force capacity (numerator of equation 3)

F is the cumulative infiltrated water (m)

FOS is the factor of safety (-)

H is the height of the flow (m)

K is the resistance parameter for laminar flow (-)

805 L is the length scale of the flow (m)

i is the root diameter class

m is the fraction of the soil depth that is saturated from the basal boundary (-)

p is the calibration factor for the critical velocity for deposition (-)

z is the elevation of the top surface (m)

810 α is the peak horizontal earthquake acceleration ($m\ s^{-2}$)

β is the slope angle (-)

γ is the density of the slope material ($kg\ m^{-3}$)

η is the viscosity ($kg\ s^{-1}\ m^{-1}$)

θ is the angle of shear distrortion in the shear zone (°)

815 ψ is the matric pressure at the wetting front ($h = \psi + Z$) (m)

ϕ is the internal friction angle (°)

References

Baartman, J. E., Jetten, V. G., Ritsema, C. J., & Vente, J. (2012a). Exploring effects of rainfall intensity and duration on soil erosion at the catchment scale using openLISEM: Prado catchment, SE Spain. *Hydrological processes*, *26*(7), 1034-1049.

Baggio, T., Mergili, M., & D'Agostino, V. (2021). Advances in the simulation of debris flow erosion: The case study of the Rio Gere (Italy) event of the 4th August 2017. *Geomorphology*, *381*, 107664

Bout, B., Van Westen, C.J., Lombardo, L & Jetten, V. (2018). Integration of two-phase solid fluid equations in a catchment model for flashfloods, debris flows and shallow slope failures. Environmental Modelling and Software, in press.

Cance, A., Thiery, Y., Fressard, M., Vandromme, R., Maquaire, O., Reid, M. E., & Mergili, M. (2017, October). Influence of complex slope hydrogeology on landslide susceptibility assessment: the case of the Pays d'Auge (Normandy, France). In *Journées Aléas Gravitaires*.

Chai, H., Liu, H., Zhang, Z., and Xu, Z. (2000): The distribution, causes and effects of damming landslides in China, Journal of the Chengdu Institute of Technology, 27, 302–307, 2000 (In Chinese).

Chen, H. X., & Zhang, L. M. (2015). EDDA 1.0: integrated simulation of debris flow erosion, deposition and property changes. *Geoscientific Model Development*, *8*(3), 829-844.

Chen, M. L., Hu, G. S., Chen, N. S., Zhao, C. Y., Zhao, S. J., & Han, D. W. (2016). Valuation of debris flow mitigation measures in tourist towns: a case study on Hongchun gully in southwest China. *Journal of Mountain Science*, *13*(10), 1867-1879.

Chok, Y. H., Jaksa, M. B., Kaggwa, W. S., & Griffiths, D. V. (2015). Assessing the influence of root reinforcement on slope stability by finite elements. *International Journal of Geo-Engineering*, *6*(1), 12.

Chow, V. (1959). *Open channel hydraulics*. McGraw-Hill Book Company, Inc; New York.

Costa, J.E., Schuster, R.L., 1988. The formation and failure of natural dams. Geological Society of America Bulletin 100, 1054-1068

Dai, F. C., Lee, C. F., Deng, J. H., & Tham, L. G. (2005). The 1786 earthquake-triggered landslide dam and subsequent dam-break flood on the Dadu River, southwestern China. *Geomorphology*, *65*(3), 205-221.

De Baets, S., Poesen, J., Reubens, B., Wemans, K., De Baerdemaeker, J., & Muys, B. (2008). Root tensile strength and root distribution of typical Mediterranean plant species and their contribution to soil shear strength. *Plant and soil*, *305*(1-2), 207-226.

845 Dhondia, J. F. and Stelling, G. S.: Application of the one dimensional-two dimensional integrated hydraulic model for flood simulation and damage assessment, Hydroinformatics 2002: Proceedings of the Fifth International Conference on Hydroinformatics, Cardiff, UK, 2002.

Ermini, L., and Casagli, N., (2003). Prediction of the behavior of landslide dams using a geomorphological dimensionless index. Earth Surface Processes and Landforms 28, 31-47.

850 Evans, S. G., 1986, The maximum discharge of outburst floods caused by the breaching of man-made and natural dams: Can. Geotch. J., v. 23, p. 385–387.

Fan, X., Tang, C. X., Van Westen, C. J., & Alkema, D. (2012). Simulating dam-breach flood scenarios of the Tangjiashan landslide dam induced by the Wenchuan Earthquake. *Natural hazards and earth system sciences*, *12*(10), 3031.

Fread, D. L. (1988). *BREACH, an erosion model for earthen dam failures*. Hydrologic Research Laboratory, National Weather
855 Service, NOAA.

Gill, J. C., & Malamud, B. D. (2014). Reviewing and visualizing the interactions of natural hazards. *Reviews of Geophysics*, *52*(4), 680-722.

Green, W. H & Ampt. GA (1911). *Studies in soil physics, J. Agric. Sci*, *4*, 1-24

Hao, H., Yang, X., Huang, Y., Liu, K., Zeng, Z., 2011. Emergency Investigation Report of Niujuan Catchment Debris Flows.
860 Unpublished Report, in Chinese. Sichuan Huadi Construction Engineering Co., Ltd.

Harp, E.L., Crone, A.J., 2006. Landslides Triggered by the October 8, 2005, Pakistan Earthquake and Associated Landslide-Dammed Reservoirs. U.S. Geological Survey Open-file Report, 2006-1052, 13

Hu, W., Dong, X. J., Xu, Q., Wang, G. H., Van Asch, T. W. J., & Hicher, P. Y. (2016). Initiation processes for run-off generated debris flows in the Wenchuan earthquake area of China. *Geomorphology*, *253*, 468-477.

51

865   Huang, Y. Y., Han, H., Tang, C., & Liu, S. J. (2017). Plant community composition and interspecific relationships among dominant species on a post-seismic landslide in Hongchun Gully, China. *Journal of Mountain Science*, *14*(10), 1985-1994.

Hungr, O., Salgado, F. M., & Byrne, P. M. (1989). Evaluation of a three-dimensional method of slope stability analysis. Canadian Geotechnical Journal, 26(4), 679-686.

870   Hungr, O., McDougall, S., & Bovis, M. (2005). Entrainment of material by debris flows. In *Debris-flow hazards and related phenomena* (pp. 135-158). Springer, Berlin, Heidelberg.

Hürlimann, M., Medina, V., Bateman A., Copons, R., Altimir J., 2007. Comparison of different techniques to analyse the mobility of debris flows during hazard assessment-Case study in La Comella catchment, Andorra. In Chen & Majors (eds.) Debris-Flow Hazard Mitigation :Mechanics, Prediction and Assessment. Millpress, Netherlands, pp. 411-422.

875   Iverson, R. M., & Ouyang, C. (2015). Entrainment of bed material by Earth-surface mass flows: Review and reformulation of depth-integrated theory. *Reviews of geophysics*, *53*(1), 27-58.

Jafarzadeh, F., Shahrabi, M. M., & Jahromi, H. F. (2015). On the role of topographic amplification in seismic slope instabilities. *Journal of Rock Mechanics and Geotechnical Engineering*, *7*(2), 163-170.

Jetten (2002). LISEM, Limburg Soil Erosion Model, User's Manual

880   Jiang, Z., Huete, A. R., Chen, J., Chen, Y., Li, J., Yan, G., & Zhang, X. (2006). Analysis of NDVI and scaled difference vegetation index retrievals of vegetation fraction. *Remote sensing of environment*, *101*(3), 366-378.

Kappes, M. S., Keiler, M., von Elverfeldt, K., & Glade, T. (2012). Challenges of analyzing multi-hazard risk: a review. *Natural hazards*, *64*(2), 1925-1958.

Kalacska, M., Sánchez-Azofeifa, G. A., Rivard, B., Calvo-Alvarado, J. C., Journet, A. R. P., Arroyo-Mora, J. P., & Ortiz-

885   Ortiz, D. (2004). Leaf area index measurements in a tropical moist forest: A case study from Costa Rica. *Remote Sensing of Environment*, *91*(2), 134-152.

Korup, O.: Geomorphic hazard assessment of landslide dams in South Westland, New Zealand: Fundamental problems and approaches, Geomorphology, 66, 167–188, 2005.

Kuriakose, S. L., Devkota, S., Rossiter, D. G., & Jetten, V. G. (2009). Prediction of soil depth using environmental variables in an anthropogenic landscape, a case study in the Western Ghats of Kerala, India. *Catena*, *79*(1), 27-38.

Lehmann, P., J. von Rütte, and D. (2017) STEP TRAMM: Landslide Triggering Model (version 2017.8). Software available at http://www.step.ethz.ch/step-tramm.html

Li, D., Hao, H., Ma, j., Wu, X., Yan, Z., Li, G., Wang, H., Gao, J., Liu, H., Huang, Y., Yang, X., Zeng, Z., Liu, J., Gao, L., Shen, T., Cao, N., Zhang, Y., Li, Z., Liu, K., Li, D., Xian, Z., 2011. Emergency Mitigation Engineering Design on the Catastrohic Hongchun Catchment Debris Flow, Yingxiu, Wenchuan County. Unpublished report, in Chinese. Guanghan Institute of Geological Engineering Investigation.

Li, M. H., Sung, R. T., Dong, J. J., Lee, C. T., & Chen, C. C. (2011). The formation and breaching of a short-lived landslide dam at Hsiaolin Village, Taiwan—Part II: Simulation of debris flow with landslide dam breach. *Engineering Geology*, *123*(1), 60-71.

Li, Y., Zhou, R., Zhao, G., Li, H., Su, D., Ding, H., & Ma, C. (2014). Tectonic uplift and landslides triggered by the Wenchuan earthquake and constraints on orogenic growth: a case study from Hongchun Gully, Longmen Mountains, Sichuan, China. *Quaternary international*, *349*, 142-152.

Liu, N., Zhang, J., Lin, W., Cheng, W., and Chen, Z.: Draining Tangjiashan Barrier Lake after Wenchuan Earthquake and the flood propagation after the dam break, Sci. China Ser. E., 52, 801–809, 2009.

Malet, J.-P., Remaître, A., Maquaire, O., 2004. Runout modeling and extension of the threatened area associated with muddy debris flows. Geomorphologie: relief, processus, environnement n.3, pp. 195-210

Mergili, M., Jan-Thomas, F., Krenn, J., & Pudasaini, S. P. (2017). r. avaflow v1, an advanced open-source computational framework for the propagation and interaction of two-phase mass flows. *Geoscientific Model Development*, *10*(2), 553.

Mergili, M., Marchesini, I., Alvioli, M., Metz, M., Schneider-Muntau, B., Rossi, M., & Guzzetti, F. (2014). A strategy for GIS-based 3-D slope stability modelling over large areas. *Geoscientific Model Development*, *7*(6), 2969-2982.

Mergili, M., Marchesini, I., Rossi, M., Guzzetti, F., & Fellin, W. (2014). Spatially distributed three-dimensional slope stability modelling in a raster GIS. Geomorphology, 206, 178–195.

Mergili, M., Emmer, A., Juřicová, A., Cochachin, A., Fischer, J. T., Huggel, C., & Pudasaini, S. P. (2018a). How well can we simulate complex hydro-geomorphic process chains? The 2012 multi-lake outburst flood in the Santa Cruz Valley (Cordillera Blanca, Perú). *Earth surface processes and landforms*, *43*(7), 1373-1389.

Mergili, M., Frank, B., Fischer, J. T., Huggel, C., & Pudasaini, S. P. (2018b). Computational experiments on the 1962 and 1970 landslide events at Huascarán (Peru) with r. avaflow: Lessons learned for predictive mass flow simulations. *Geomorphology*, *322*, 15-28.

Mohadjer, S., Ehlers, T. A., Bendick, R., Stübner, K., & Strube, T. (2016). A Quaternary fault database for central Asia. *Natural Hazards and Earth System Sciences*, *16*(2), 529.

Morgan, R. P. C., Quinton, J. N., Smith, R. E., Govers, G., Poesen, J. W. A., Auerswald, K., ... & Styczen, M. E. (1998). The European Soil Erosion Model (EUROSEM): a dynamic approach for predicting sediment transport from fields and small catchments. *Earth Surface Processes and Landforms: The Journal of the British Geomorphological Group*, *23*(6), 527-544.

Morgenstern, N. R., & Sangrey, D. A. (1978). Methods of stability analysis. *Transportation Research Board Special Report*, (176).

Nash. T, Bell. D, Davies. T, Nathan. S, 2008. Analysis of the formation and failure of Ram Creek landslide dam, South Island, New Zealand. New Zealand Journal of Geology & Geophysics 51, 187-193.

Nearing, M. A., Ascough, L. D., & Chaves, H. M. L. (1989). WEPP model sensitivity analysis. *Water erosion prediction project landscape profi le model documentation. NSERL Report*, (2).

Newmark, N. M. (1965). Effects of earthquakes on dams and embankments. *Geotechnique*, *15*(2), 139-160.

O'brien, J. S., Julien, P. Y., & Fullerton, W. T. (1993). Two-dimensional water flood and mudflow simulation. *Journal of hydraulic engineering*, *119*(2), 244-261.

Ouyang, C., He, S., & Tang, C. (2015). Numerical analysis of dynamics of debris flow over erodible beds in Wenchuan earthquake-induced area. *Engineering Geology*, *194*, 62-72.

Peng, M., and Zhang, L. M., 2012, Breaching parameters of landslide dams: Landslides, v. 9, no. 1, p. 13-31.

Pix4D, S. A. (2017). Pix4dmapper 3.2 user manual.

Pudasaini, S. P. (2012). A general two-phase debris flow model. *Journal of Geophysical Research: Earth Surface*, *117*(F3).

940 Pudasaini, S. P., & Fischer, J. T. (2016). A mechanical erosion model for two-phase mass flows. *arXiv preprint arXiv:1610.01806*.

Pyke, R., 1991. TSLOPE3: User Guide. Taga Engineering System and Software, Lafayette.

Reid, M. E., Christian, S. B., Brien, D. L., & Henderson, S. . (2015). Scoops3D—Software to Analyze Three-Dimensional Slope Stability Throughout a Digital Landscape. In U.S. Geological Survey Techniques and Methods, book 14 (p. 218).

945 https://doi.org/10.3133/tm14A1

Rickenmann, D., Laigle, D. McArdell, B.W., Hübl, J.. 2006. Comparison of 2D debris-flow simulation models with field events. Computat Geosci, 10, pp. 241-264

Roelvink, J. A., & Van Banning, G. K. F. M. (1995). Design and development of DELFT3D and application to coastal morphodynamics. *Oceanographic Literature Review*, *11*(42), 925.

950 Ruette, J. V., Lehmann, P., & Or, D. (2013). Rainfall-triggered shallow landslides at catchment scale: Threshold mechanics-based modeling for abruptness and localization. *Water Resources Research*, *49*(10), 6266-6285.

Saxton, K. E., & Rawls, W. J. (2006). Soil water characteristic estimates by texture and organic matter for hydrologic solutions. *Soil Science Society of America Journal*, *70*(5), 1569-1578.

Schuster, R.L. (1993) Landslide dams – a worldwide phenomenon. Proceedings Annual Symposium of The Japanese Landslide

955 Society, Kansai Branch, 27 April, Osaka, 1–23.

Schmidt, K. M., Roering, J. J., Stock, J. D., Dietrich, W. E., Montgomery, D. R., & Schaub, T. (2001). The variability of root cohesion as an influence on shallow landslide susceptibility in the Oregon Coast Range. *Canadian Geotechnical Journal*, *38*(5), 995-1024.

Singh, K. P., & Snorrason, A. (1984). Sensitivity of outflow peaks and flood stages to the selection of dam breach parameters

960 and simulation models. *Journal of hydrology*, *68*(1-4), 295-310.

Smith, R. E., & Parlange, J. Y. (1978). A parameter-efficient hydrologic infiltration model. *Water Resources Research*, *14*(3), 533-538.

Stokes, G. G. (1850). On the effect of internal friction of fluids on the motion of pendulums. *Trans. Camb. phi1. S0c*, *9*(8), 106.

965   Swanson, F. J., Oyagi, N., and Tominaga, M.: Landslide dams in Japan, in: Landslide dams: process, risk, and mitigation New York: American Society of Civil Engineers Special Publication, edited by: Schuster, R. L., No. 3, 273–378, 1986.

Tang, C., Zhu, J., Ding, J., Cui, X. F., Chen, L., & Zhang, J. S. (2011). Catastrophic debris flows triggered by a 14 August 2010 rainfall at the epicenter of the Wenchuan earthquake. *Landslides*, *8*(4), 485-497.

Tang, C., Jiang, Z., & Li, W. (2015). Seismic landslide evolution and debris flow development: a case study in the Hongchun

970   Catchment, Wenchuan area of China. In *Engineering Geology for Society and Territory-Volume 2* (pp. 445-449). Springer, Cham.

Tang, C., Van Westen, C. J., Tanyas, H., & Jetten, V. G. (2016). Analysing post-earthquake landslide activity using multi-temporal landslide inventories near the epicentral area of the 2008 Wenchuan earthquake. *Natural hazards and earth system sciences*, *16*(12), 2641.

975   Tang, C., Tanyas, H., van Westen, C. J., Tang, C., Fan, X., & Jetten, V. G. (2019). Analysing post-earthquake mass movement volume dynamics with multi-source DEMs. *Engineering Geology*, *248*, 89-101.

Takahashi, T., Nakagawa, H., Harada, T., and Yamashiki, Y.: Routing debris flows with particle segregation, J. Hydraul. Eng., 118, 1490–1507, 1992.

Tun, Y. W., Llano-Serna, M. A., Pedroso, D. M., & Scheuermann, A. (2019). Multimodal reliability analysis of 3D slopes

980   with a genetic algorithm. *Acta Geotechnica*, *14*(1), 207-223.

Valiani, A., Caleffi, V., & Zanni, A. (2002). Case study: Malpasset dam-break simulation using a two-dimensional finite volume method. *Journal of Hydraulic Engineering*, *128*(5), 460-472.

Van Asch, Th.W.J., Malet, J.-P., van Beek, L.P.H., Amitrano, D., (2007). Techniques, issues and advances in numerical modelling of landslide hazard. Bull. Soc. géol. Fr., 2007, t. 178, no 2, pp. 65-88.

985   Van Leer, B. (1979). Towards the ultimate conservative difference scheme. V. A second-order sequel to Godunov's method. *Journal of computational Physics*, *32*(1), 101-136.

van Westen, C. J. & Greiving, S. (2017) Risk Assessment for Decision Making. Environmental hazards Methodologies for Risk Assessment and Management. Dalezios, N. R. (ed.). p. 31-94

Wald, D. J., Worden, B. C., Quitoriano, V., & Pankow, K. L. (2005). *ShakeMap manual: technical manual, user's guide, and software guide* (No. 12-A1).

Walder, J. S. and O'Connor, J. E. (1997) Methods for predicting peak discharge of floods caused by failure of natural and constructed earthen dams, Water Resour. Res., 33, 2337–48, 1997.

Wang, G., Liu, F., Fu, X., & Li, T. (2008). Simulation of dam breach development for emergency treatment of the Tangjiashan Quake Lake in China. *Science in China Series E: Technological Sciences*, *51*, 82-94.

Wasowski, J., Keefer, D. K., & Lee, C. T. (2011). Toward the next generation of research on earthquake-induced landslides: current issues and future challenges. *Engineering Geology*, *122*(1-2), 1-8.

Xie, M. W., Esaki, T., Zhou, G. Y., & Mitani, Y. (2003). Three-dimensional stability evaluation of landslides and a sliding process simulation using a new geographic information systems component. Environmental Geology, 43(5), 503–512. https://doi.org/10.1007/s00254-002-0655-3

Yang, J., 2010. Emergency Investigation Report of Shaofang Catchment Debris Flows. Unpublished report, in Chinese. Sichuan Institute of Geological Engineering Investigation.

Zhang, N., Matsushima, T., & Peng, N. (2018). Numerical investigation of post-seismic debris flows in the epicentral area of the Wenchuan earthquake. *Bulletin of Engineering Geology and the Environment*, 1-16.

Zhu, Y. (2006). *Breach growth in clay-dikes* (Doctoral dissertation, TU Delft, Delft University of Technology).